JOURNAL OF PETROLOGY | VOLUME 46 | NUMBER 6 | PAGES 1085–1119 | 2005 | doi:10.1093/petrology/egi011

Mesoproterozoic Reworking of Palaeoproterozoic Ultrahigh-temperature Granulites in the Central Indian Tectonic Zone and its Implications

S. K. BHOWMIK[1]*, A. BASU SARBADHIKARI[1], B. SPIERING[2] AND M. M. RAITH[2]

[1]DEPARTMENT OF GEOLOGY AND GEOPHYSICS, INDIAN INSTITUTE OF TECHNOLOGY, KHARAGPUR-721 302, INDIA

[2]MINERALOGISCH–PETROLOGISCHES INSTITUT, DER UNIVERSITÄT BONN, POPPELSDORFER SCHLOß, D-53115 BONN, GERMANY

RECEIVED OCTOBER 4, 2003; ACCEPTED DECEMBER 14, 2004
ADVANCE ACCESS PUBLICATION FEBRUARY 4, 2005

*In the southern periphery of the Sausar Mobile Belt (SMB), the southern component of the Central Indian Tectonic Zone (CITZ), a suite of felsic and aluminous granulites, intruded by gabbro, noritic gabbro, norite and orthopyroxenite, records the polymetamorphic evolution of the CITZ. Using sequences of prograde, peak and retrograde reaction textures, mineral chemistry, geothermobarometric results and petrogenetic grid considerations from the felsic and the aluminous granulites and applying metamorphosed mafic dyke markers and geochronological constraints, two temporally unrelated granulite-facies tectonothermal events of Pre-Grenvillian age have been established. The first event caused ultrahigh-temperature (UHT) metamorphism (M_1) (*T *$\sim$ 950°C) at relatively deeper crustal levels (*P *$\sim$ 9 kbar) and a subsequent post-peak near-isobaric cooling* P–T *history (M_2). M_1 caused pervasive biotite-dehydration melting, producing garnet–orthopyroxene and garnet–rutile and sapphirine–spinel-bearing incongruent solid assemblages in felsic and aluminous granulites, respectively. During M_2, garnet–corundum and later spinel–sillimanite–biotite assemblages were produced by reacting sapphirine–spinel–sillimanite and rehydration of garnet–corundum assemblages, respectively. Applying electron microprobe (EMP) dating techniques to monazites included in M_1 garnet or occurring in low-strain domains in the felsic granulites, the UHT metamorphism is dated at 2040–2090 Ma. Based on the deep crustal heating–cooling* P–T *trajectory, the authors infer an overall counterclockwise* P–T *path for this UHT event. During the second granulite event, the Palaeoproterozoic granulites experienced crustal attenuation to $\sim$6·4 kbar at* T *$\sim$ 675°C during M_3 and subsequent near-isothermal loading to $\sim$8 kbar during M_4. In the felsic granulites, the former is marked by decomposition of M_1 garnet to orthopyroxene–plagioclase symplectites. During M_4, there was renewed growth of garnet–quartz symplectites in the felsic granulites, replacing the M_3 mineral assemblage and also the appearance of coronal garnet–quartz–clinopyroxene assemblages in metamorphosed mafic dykes. Using monazites from metamorphic overgrowths and metamorphic recrystallization domains from the felsic granulite, the M_4 metamorphism is dated at 1525–1450 Ma. Using geochronological and metamorphic constraints, the authors interpret the M_3–M_4 stages to be part of the same Mesoproterozoic tectonothermal event. The result provides the first documentation of UHT metamorphism and Palaeo- and Mesoproterozoic metamorphic processes in the CITZ. On a broader scale, the findings are also consistent with the current prediction that isobarically cooled granulites require a separate orogeny for their exhumation.*

KEY WORDS: *Central Indian Tectonic Zone; UHT metamorphism; counterclockwise* P–T *path; monazite chemical dating*

INTRODUCTION

The majority of orogens are tectonic collages of a number of elongated lithotectonic domains with contrasting

*Corresponding author. E-mail: santanu@gg.iitkgp.ernet.in

tectonothermal histories (e.g. Grenville orogen: Rivers *et al.*, 1989; Eastern Ghats Mobile Belt: Dobmeier & Raith, 2003). The key to unravelling ancient orogenic processes is, thus, to identify these domains and to reconstruct the metamorphic *P–T–t* paths of rocks within them. Careful reconstruction of metamorphic *P–T–t* paths in these domains is expected to reveal their polycyclic nature. Such polymetamorphic history has been documented from basement inliers in some orogens (e.g. Chewore Inliers, in the Zambezi belt, Zimbabwe: Goscombe *et al.*, 1998; Ungava orogen, Canada: St-Onge & Ijewliw, 1996). One of the locales where polymetamorphic rocks could exist as a distinct metamorphic belt is the so-called allochthonous polycyclic domain in an orogen (Rivers *et al.*, 1989). The present study is from one such allochthonous polycyclic domain in the Sausar Mobile belt (SMB), which constitutes the southern component of the composite Central Indian Tectonic Zone (CITZ) (Fig. 1). In recent reconstructions of East Gondwanaland, the CITZ is recognized as an important Proterozoic collisional zone, along which the North Indian Block (NIB: Eriksson *et al.*, 1999; comprising the Aravalli–Bundelkhand Provinces) and the South Indian Block (SIB; comprising the Singhbhum, Bastar and Dharwar Provinces) were amalgamated during the Palaeoproterozoic to form the Indian subcontinent (Yedekar *et al.*, 1990; Jain *et al.*, 1991; Mishra *et al.*, 2000). However, there is insufficient petrological and geochronological evidence in support of this. The recent discovery of a high-pressure upper amphibolite–granulite-facies domain (locally referred to as the Ramakona–Katangi granulite (RKG) domain, Fig. 1) in the northern part of the SMB has led to the suggestion that this belt marks a major, Grenville-aged, collisional event during the final amalgamation of the SIB and the NIB (Bhowmik & Roy, 2003; Bhowmik & Spiering, 2004). The present study is from another such domain [Bhandara Balaghat granulite (BBG) domain, Fig. 1] in the southern part of the SMB. The authors have used reaction textures, mineral chemistry, geothermobarometric results and petrogenetic grid considerations from felsic granulites, aluminous granulites and mafic dyke markers, and geochronological data, to elucidate polymetamorphic events, separated in age by ~500 Ma. In the process, a Palaeoproterozoic ultrahigh-temperature (UHT) metamorphism has been recognized for the first time in the CITZ. The implications of these new findings in the context of the evolutionary history of orogens in general, and of the CITZ in particular, are discussed. Mineral abbreviations are after Kretz (1983).

GEOLOGICAL SETTING

The BBG domain is an allochthonous tectonic sheet between the low-grade (greenschist-facies) Sausar Group of rocks in the north and the cratonic domain of low- to medium-grade felsic gneisses of the Amgaon gneissic complex on the south (Bhowmik & Pal, 2000; Bhowmik & Roy, 2003; Fig. 2a). Both the northern and the southern margins of the BBG domain are highly tectonized (Fig. 2a). The BBG domain is lensoidal in shape, nearly 190 km long and 4–20 km wide, and tapers towards both east and west (Fig. 1). The lithological ensemble can be subdivided into four distinct components (Fig. 2a): (1) a large part of the domain is occupied by a migmatitic felsic gneiss (locally with garnet) of tonalitic to granodioritic composition; (2) enclaves of garnet–cordierite gneiss, iron-formation granulite, quartzite, aluminous granulite and felsic granulite occur within the felsic gneiss; (3) a mafic–ultramafic magmatic suite of metagabbro, metanoritic gabbro, metanorite and metaorthopyroxenite occurs as concordant sheets in the felsic gneiss; (4) mafic dykes of metagabbronorite and metaolivine gabbro (termed Md_1) and amphibolite (termed Md_2).

The BBG domain records five phases of deformation (BD_1–BD_5, where B refers to the BBG domain), the earliest of which is preserved as relict high-*T* granulite facies banding (BS_1), demarcated by alternate light- and dark-coloured migmatitic layers in the felsic and aluminous granulites (Figs 3 and 4). BD_2 is preserved as a rare BS_2 fabric in the felsic granulite (Fig. 4). This was followed by a strong ductile shear zone deformation (BD_3) that produced southerly verging isoclinal folds (BF_3) and a strong mylonitic fabric (BS_3) (Fig. 4). The mafic dykes Md_1 were folded by BF_3. A southerly tectonic transport at relatively high temperatures during BD_3 is indicated by sigma-type asymmetrical orthopyroxene porphyroclasts and the southerly vergence of the BF_3 folds. Subsequent deformation (BD_4) produced narrow, steep, ductile shear-zone fabrics that are mostly restricted to the margins of the BBG domains. Md_2 mafic dykes are folded only by BF_4. Geological mapping across the BBG domain–Sausar Group supracrustal contact (Fig. 1) showed that the BS_4 fabric could be correlated with the earliest deformational fabric in the latter. The terminal deformation BD_5 produced cross-folds both in the Sausar Group rocks and rocks in the BBG domain.

The samples of felsic granulites have been collected from two structurally equivalent locations from the southern part of the BBG domain: (1) Larsara in the east; (2) Dongariya in the west (Fig. 2a). In both the locations, felsic granulites are interlayered with metagabbros and iron-formation granulites. Aluminous granulites and Md_1 have been sampled from the Larsara area only (Fig. 2b). The felsic granulites occur as ~750 m long and ~100 m wide northeast–southwest-trending bodies, bounded on both sides by the metabasites. The mylonite foliation, BS_3, which is best

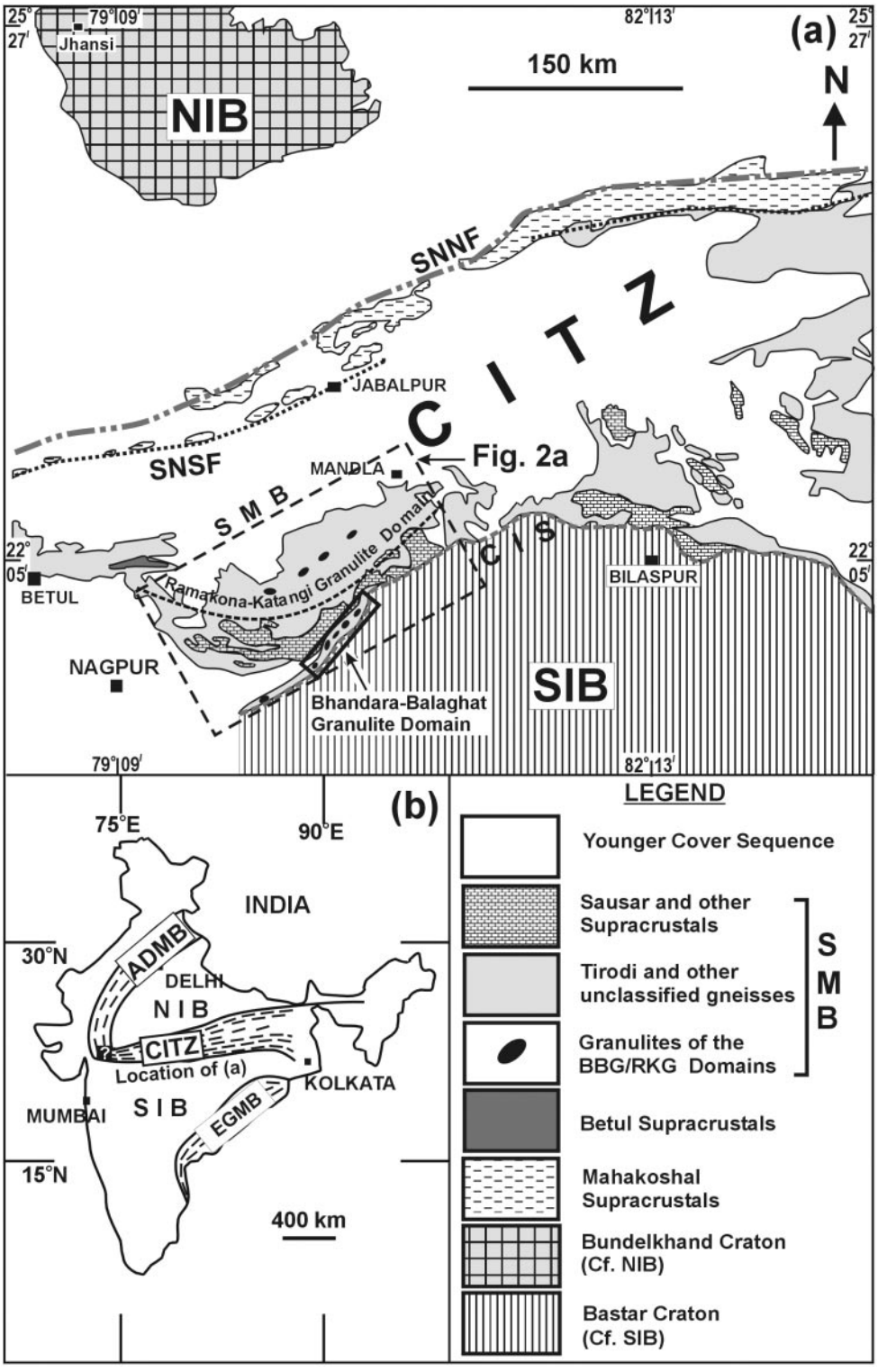

Fig. 1. Distribution of the different lithotectonic components in the Central Indian Tectonic Zone (CITZ) between the North Indian Block (NIB) and the South Indian Block (SIB). The Sausar mobile belt (SMB), which occurs in the southern part of the CITZ (shown by dashed rectangle) comprises two granulite domains: the Ramakona–Katangi granulite (RKG) domain in its northern and the Bhandara–Balaghat granulite (BBG) domain in its southern margins. The box shows the location of the study area in the BBG domain (detailed map shown in Fig. 2a). The inset shows the location of the CITZ in the tectonic framework of Peninsular India. EGMB (Eastern Ghats Mobile Belt) and ADMB (Aravalli–Delhi Mobile Belt) represent two contiguous mobile belts.

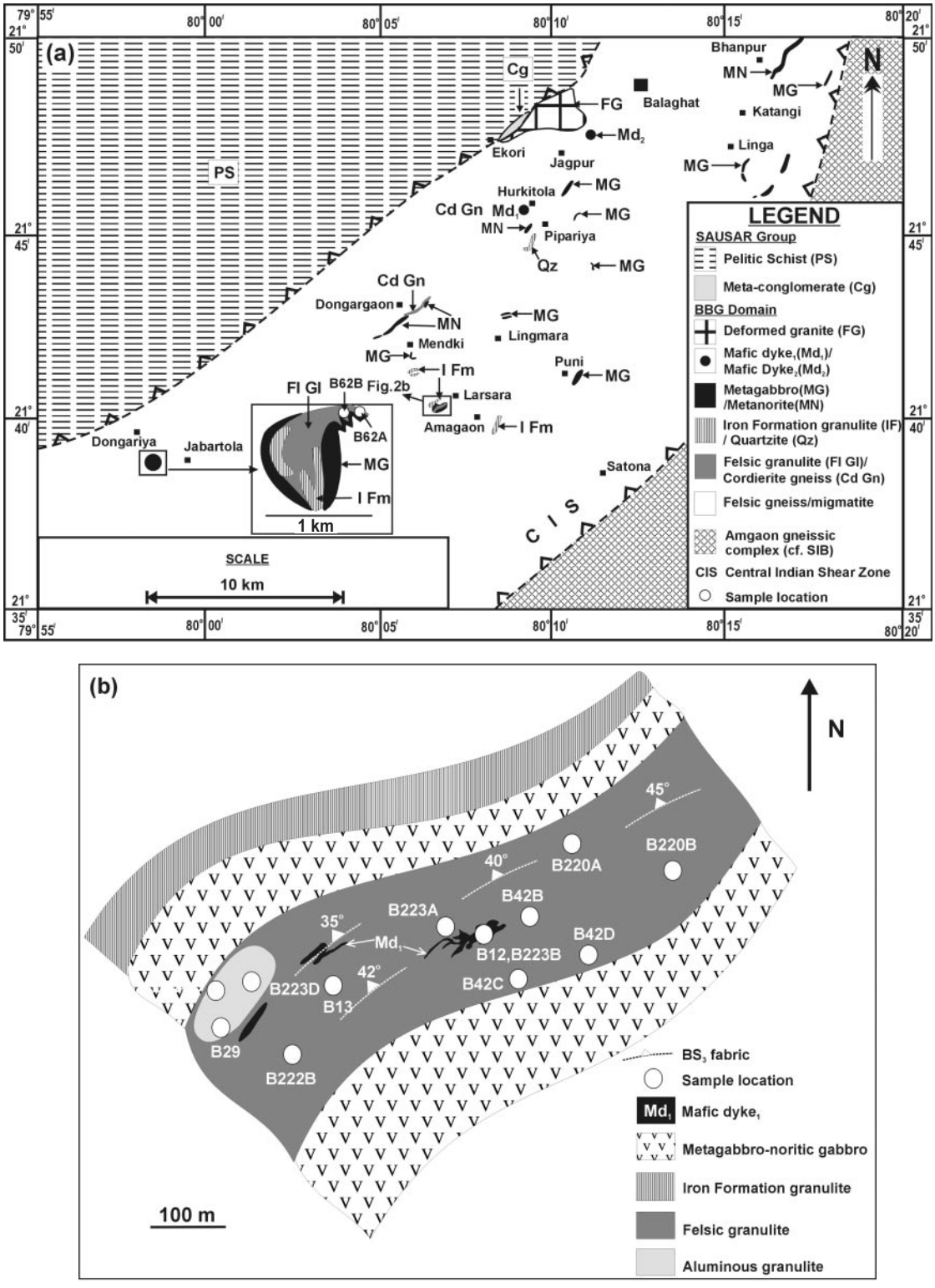

Fig. 2. (a) Simplified map of the Bhandara–Balaghat granulite domain in the SMB, showing the locations of the granulite occurrences. Also shown are the locations of the two study areas: Larsara in the east and Dongariya in the west. For the latter, sample locations of the felsic granulites are shown. (b) Outcrop sketch of Larsara area, showing the distribution of the interlayered sequence of felsic granulites–metagabbro–metanoritic gabbro–iron-formation granulite–aluminous granulite and mafic dyke$_1$ (Md$_1$). Also shown are the sample locations of the felsic granulites, aluminous granulites and Md$_1$.

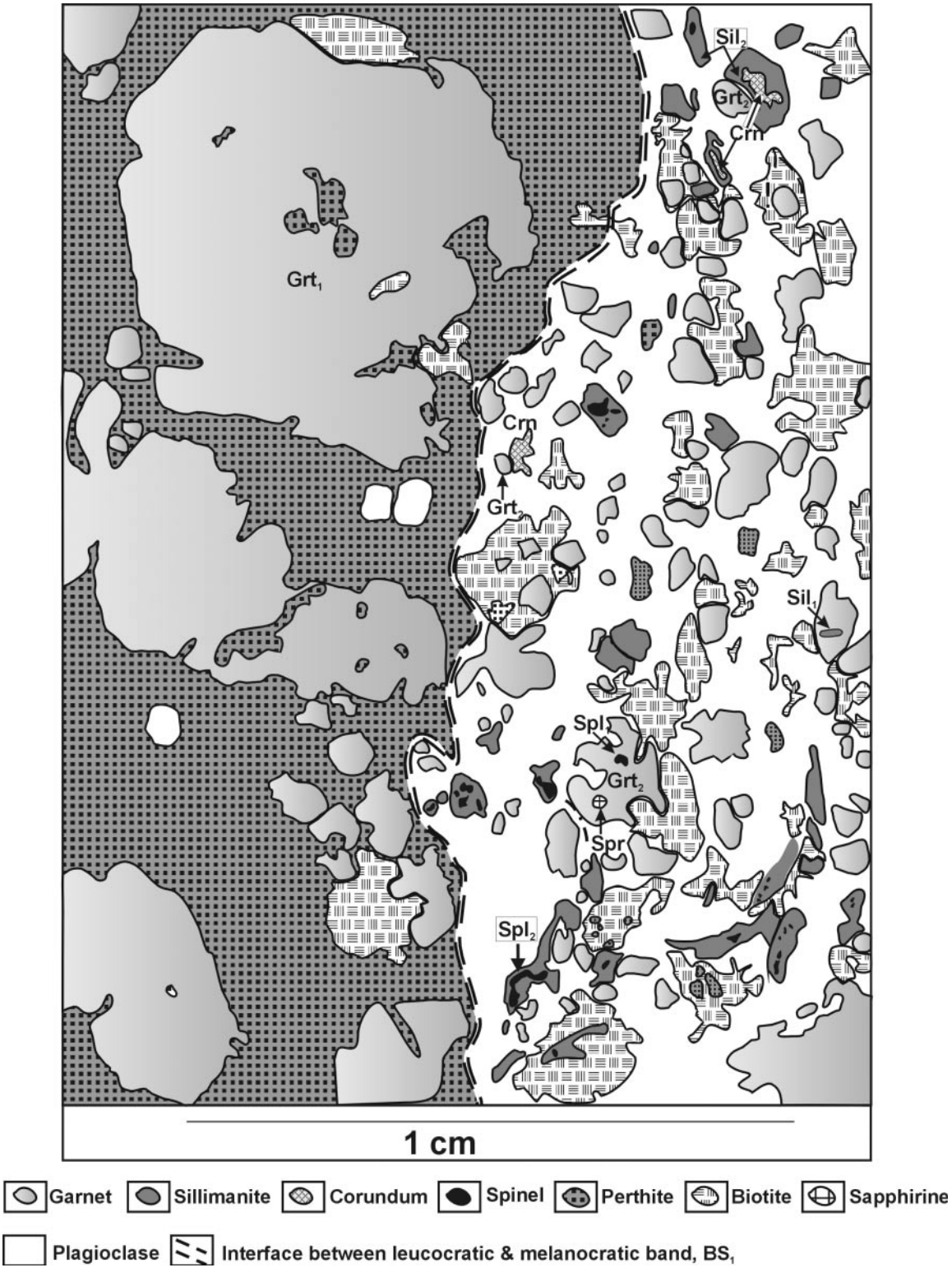

Fig. 3. Thin section sketch of an aluminous granulite. The compositional layering demarcated by the leucocratic band (to the left), and comprising porphyroblastic garnet + mesoperthite ± plagioclase ± biotite and melanocratic band (to the right), containing garnet–spinel–sillimanite–corundum–sapphirine–plagioclase–biotite assemblages, denotes the earliest recognizable granulite-facies fabric, BS_1 (B for BBG domain). In the latter band, a coarse coronal variety of garnet is dominant and includes early generation spinel (Spl_1), sillimanite (Sil_1) and sapphirine. Grt_2 is later replaced by second-generation spinel (Spl_2)–sillimanite (Sil_2)–biotite (Bt_2) coronas and symplectites, locally against Crn.

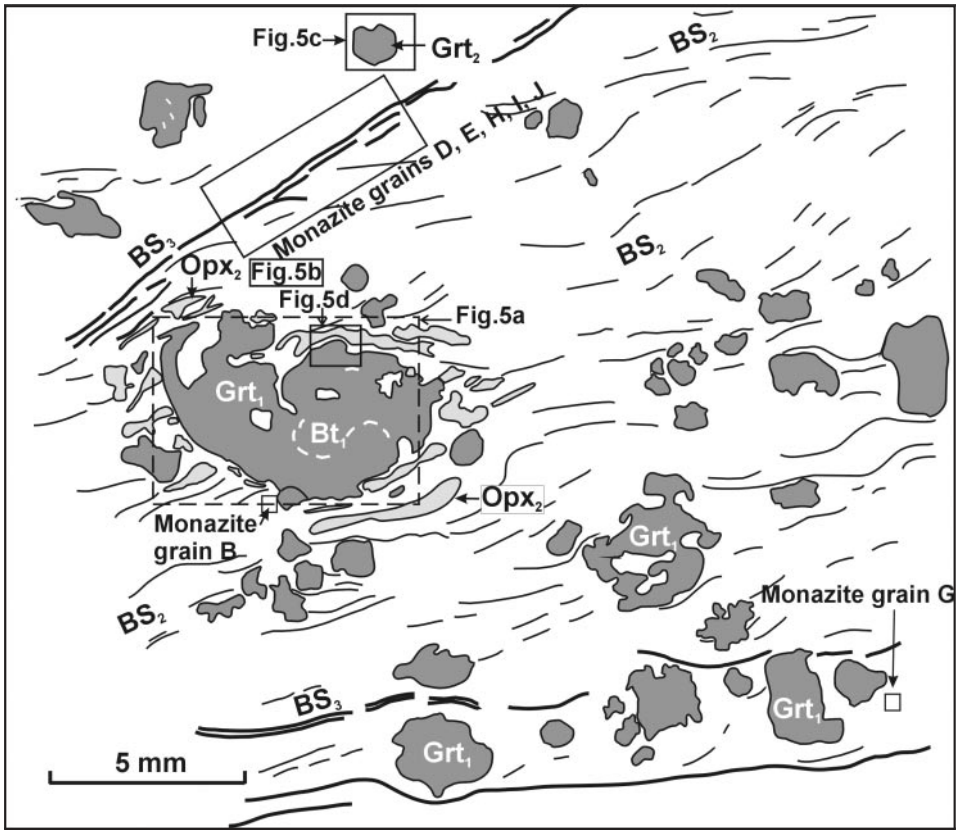

Fig. 4. Thin section sketch of felsic granulite, showing mineralogical evolution in relation to fabric development. Porphyroblastic garnet (Grt_1), occurring in a mosaic of quartzofeldspathic matrix (white portion), is armoured by a halo of orthopyroxene–plagioclase symplectites (termed Opx_2–Pl_2; see text for details). The symplectites are aligned parallel to the BS_2 fabric. BS_2 is later transposed by a strong ductile shear zone fabric, BS_3. The boxes indicate the locations of key reaction textures, shown in detail in Fig. 5. Also shown are the locations of the monazites in different textural sites used for electron microprobe dating.

developed in the felsic granulites strikes northeast–southwest and dips moderately (35–45°) towards the northwest. Aluminous granulite occurs as 10 m long and 5 m wide lensoidal bodies within the felsic granulites, in close proximity to the metagabbros. Md_1 occurs as thin veins, stringers (1–2 cm wide) and bands (~50 m wide) within the felsic granulites. The BD_3 deformation largely obliterated its intrusive relationship. However, discordant relationships in the form of thin veins and apophyses of the basic rock are still recognizable in some low-strain domains (Fig. 2b).

Sample locations for petrological studies in the Larsara area are shown in Fig. 2b. In the Dongariya area, samples of felsic granulites were taken from an identical BS_3 foliation domain. From each locality, a number of samples have been collected [numbered as B220(1), B220(2), etc. for location B220, for example]. A total of 15 samples (nine felsic granulites, four aluminous granulites and two Md_1) were selected for detailed study after scrutinizing 30 samples. The mineral associations in these samples are listed in Table 1.

PETROGRAPHY

Felsic granulite

The felsic granulite preserves a porphyroblastic assemblage of garnet, orthopyroxene, quartz, mesoperthite, plagioclase/mesoantiperthite with minor amounts of monazite, zircon and rare apatite (Fig. 5a–c). In order to differentiate them from later-generation parageneses, the porphyroblastic garnet, orthopyroxene and plagioclase are referred to as $garnet_1$, $orthopyroxene_1$ and $plagioclase_1$, respectively. $Garnet_1$ contains inclusions of biotite, quartz (Fig. 5a) and plagioclase. Biotite is totally absent in the leucosome that contains quartz, mesoperthite and plagioclase with scattered grains of $garnet_1$ and $orthopyroxene_1$.

$Garnet_1$ is partially rimmed by a symplectite of $orthopyroxene_2$–$plagioclase_2$, mostly as a collar around garnet (Figs 4 and 5a), against quartz. In some cases, the symplectite advances well within the garnet interior (Fig. 5a). The symplectites in the pressure shadow zones around $garnet_1$ are aligned parallel to the BS_2 fabric (Fig. 4), which implies that the garnet breakdown is

Table 1: Mineralogy of felsic and aluminous granulites and mafic dyke$_1$

Sample	Grt	Qtz	Kfs/Per	Pl/AP	Bt	Opx	Ru	Sil	Spl	Crn	Spr	Cpx	Ilm	Important textures
Larsara area														
Felsic granulites														
B220A(1)	+	+	+	+	+	+								A,B,D
B220A(2)	+	+	+	+	+	+								A,B,C,D
B220A(3)	+	+	+	+	+	+								A,B,E
B220B		+	+	+	+	+								A
B222B(1)	+	+	+	+	+	+								A,B
B222B(2)	+	+	+	+	+	+								A,B
B223A(1)	+	+	+	+	+	+								A,B
B223A(2)	+	+	+	+	+	+								A,B,C,D,E
B223A(3)	+	+	+	+	+	+								A,B,E
B13	+	+	+	+	+									A,B
B42D	+	+	+	+	+	+								A,B,C,D
B42B(1)	+	+	+	+	+	+							+	A,B
B42B(2)	+	+	+	+	+	+								A,B,D,E
Dongariya area														
B62A(1)	+	+	+	+	+	+								A,D
B62A(2)	+	+	+	+	+	+								A,B,D
B62A(3)	+	+	+	+	+	+								A,B,D
B62B	+	+	+	+	+	+							+	A,B,C
Larsara area														
Aluminous granulite														
B42C	+	+	+	+	+		+							G,H,I,K
B220D(1)	+		+	+	+			+	+	+	+			G,H,J,K,L,M,N
B220D(2)	+		+	+	+			+	+	+				G,H,J,K,L,M,N
B220D(3)	+		+	+	+			+	+	+	+			G,H,K,L,M,N
B220D(4)	+		+	+	+			+	+	+	+			G,H,K,L,M,N
B220D(5)	+		+	+	+			+	+	+	+			G,H,K,L,M,N
B223D(1)	+	+	+	+	+		+	+						G,H,I,K
B223D(2)	+	+	+	+	+		+	+						G,H,I,K
B29(1)	+		+	+	+			+	+	+	+			G,H,J,K,L,M,N
B29(2)	+		+	+	+			+	+	+				G,H,I,L,N
Mafic dyke, Md$_1$														
B223B	+	+		+		+						+	+	F
B12	+	+		+		+						+	+	F

Mineral abbreviations used in this and other tables are after Kretz (1983), unless mentioned; Per, perthite; AP, antiperthite. Felsic granulites: A, presence of porphyroblastic assemblages of Grt_1, Opx_1, perthite and Pl/mesoantiperthite; B, presence of Bt_1, Pl_1 and Qtz inclusions within Grt_1; C, Grt_1 decomposed to Opx_2-Pl_2 symplectites; D, metamorphic overgrowth of Grt_2-Qtz symplectites on Grt_1; E, idioblastic Grt_2, overgrowing BS_3 mylonitic fabric. Metabasic $dyke_1$: F, coronal Grt + Qtz ± Cpx assemblage replacing Opx, Cpx and Pl. Aluminous granulites: G, presence of Grt_1-Mesoperthite ± Qtz in leucocratic layers; H, presence of Bt_1 and Sil_1 inclusions within Grt_1; I, presence of Ru included within Grt_1 and also in the matrix of leucocratic layer; J, inclusion of green Spl_1 in mesoperthites; K, Bt ± Pl-bearing symplectites replacing Grt_1 against perthites in the leucocratic layer; L, presence of Spl_1, Spr and Sil_1 inclusions within Grt_2 in the melanocratic layer; M, Spl_1 included within Crn in the melanocratic layer; N, $Spl_2-Sil_2-Bt_2$ symplectites replacing Grt_2 and Crn.

broadly synkinematic with respect to BD_2. The orthopyroxene$_2$–plagioclase$_2$ symplectite is replaced by a coronal variety of garnet (garnet$_2$) interwoven with granular quartz (Fig. 5d). Garnet$_2$ is preferentially localized as an overgrowth on garnet$_1$ (Fig. 5d). Garnet$_2$ is compositionally distinct from garnet$_1$ (discussed later). Another type of garnet in the felsic granulite is of rather small size, equant in shape (Fig. 5c), and is compositionally

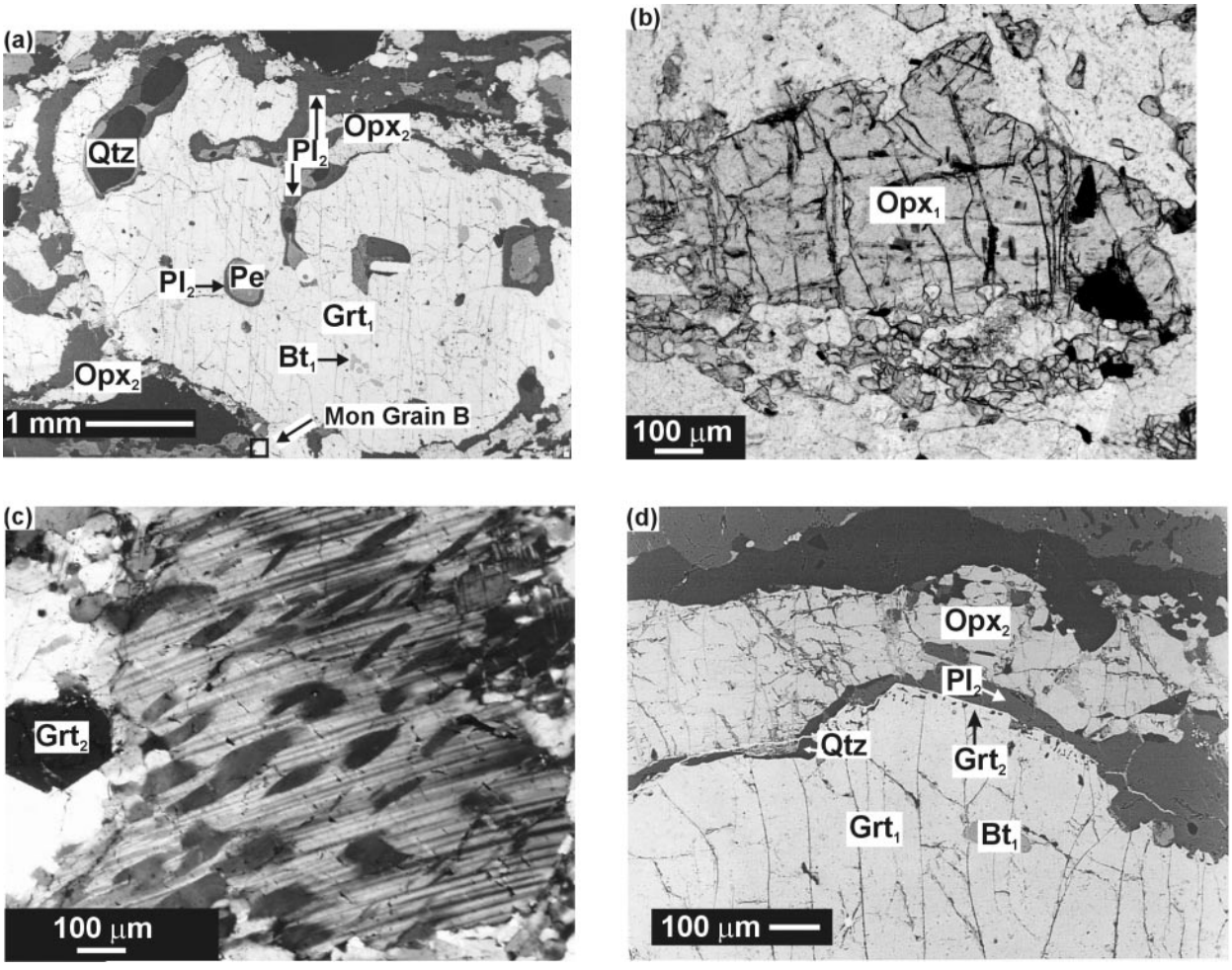

Fig. 5. Back-scattered electron images (a) and (d) and photomicrographs (b) and (c), showing textures of different stages of metamorphism in the felsic granulite. (a) Porphyroblastic Grt (Grt_1) contains inclusions of prograde Bt (Bt_1) and perthite (Pe). It is armoured by coarse Opx_2–Pl_2 symplectites, which also advance into the Grt interior. The symplectites contain inclusions of Qtz. (b) Porphyroblastic Opx (Opx_1) is armoured by recrystallized aggregates of small, strain-free, Opx grains. (c) Mesoantiperthite porphyroclast showing post-exsolution recrystallization textures. The recrystallized Pl grains (to the left) are free of exsolution lamellae. Second-generation Grt (Grt_2) with idioblastic habit has overgrown these recrystallized Pl grains. (d) Details of Fig. 5a, showing Grt_2–Qtz symplectites as metamorphic overgrowth on Grt_1, and replacing Opx_2–Pl_2 symplectites.

similar to $garnet_2$. This garnet overgrows the mylonitic foliation BS_3. By analogy, $garnet_2$ is taken to be post-BD_3.

Aluminous granulites

A porphyroblastic garnet ($garnet_1$)–mesoperthite–rutile–quartz ± sillimanite ± plagioclase ± spinel ($spinel_1$) association is present in the leucocratic layers of the aluminous granulites (Figs 3, 6a and b). $Garnet_1$ includes scattered grains of $biotite_1$ and $sillimanite_1$ (Fig. 6a), whereas mesoperthite contains rare inclusions of $spinel_1$ (Fig. 6b). Rutile occurs both within garnet and also in the matrix, often in coarse aggregates. Late biotite–plagioclase intergrowths replace $garnet_1$ against perthite.

The mineral association in the melanocratic bands is garnet–spinel–sillimanite–sapphirine–plagioclase–perthite–biotite–corundum, in the total absence of quartz (Figs 3 and 6c–f). Porphyroblastic garnet ($garnet_1$) contains inclusions of $biotite_1$ that is also present in the matrix. Sapphirine, $spinel_1$ and $sillimanite_1$ are often rimmed by a coarse coronal variety of garnet, designated as $garnet_2$ (Fig. 6c and d) (see later). Porphyroblastic sillimanite (Sil_1) additionally occurs as coarse idioblastic minerals in the melanocratic matrix. Idioblastic corundum, containing rare inclusions of $spinel_1$, is separated from $garnet_2$ by an intergrowth of $spinel_2$–$sillimanite_2$ ± $biotite_2$ (Fig. 6e). In the latter case, $spinel_2$ is preferentially concentrated at the interface of corundum, whereas $sillimanite_2$ occurs around garnet. $Biotite_2$–$spinel_2$–$sillimanite_2$ symplectites also occur as kelyphitic rims around $garnet_2$ (Fig. 6f).

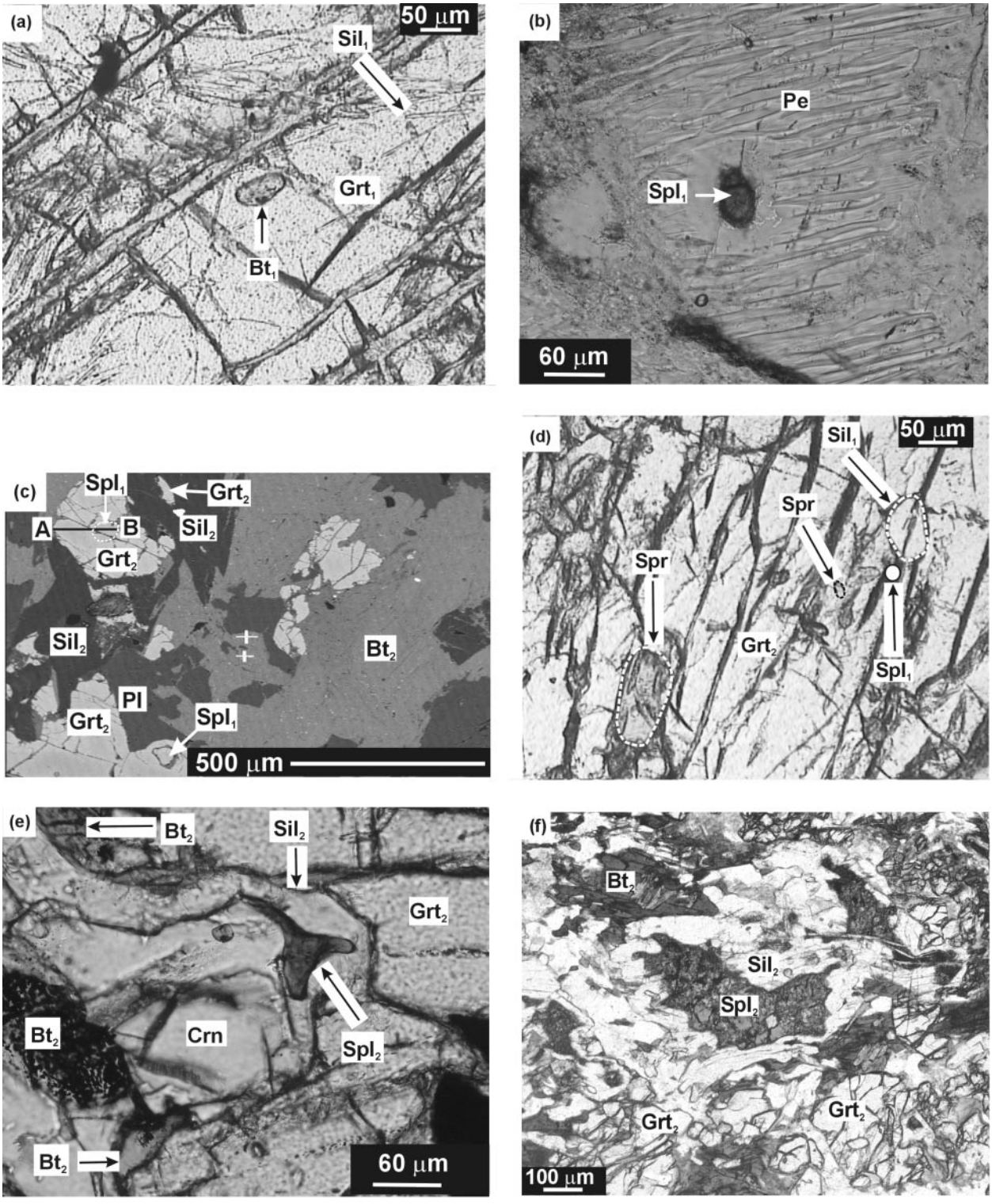

Fig. 6. Photomicrographs (a) and (b) and (d)–(f) and back-scattered electron image (c), showing reaction textures in aluminous granulites. (a) Porphyroblastic grt (Grt_1) contains inclusions of prograde Bt (Bt_1) and sillimanite (Sil_1). (b) Inclusion of early generation Spl (Spl_1) within mesoperthites (Pe). (c) Coronal Grt (Grt_2) with partially preserved idioblastic habit contains inclusion of ovoid Spl_1 in the melanocratic layer. Grt_2 is rimmed by second-generation Sil (Sil_2) and Bt (Bt_2). Sil_2 contains relict Grt within it. A–B is the location of the X_{Mg} compositional profile, shown in Fig. 10b. (d) Coarse Grt_2 contains inclusion of Spr, Spl_1 and Sil_1. (e) Formation of Spl_2–Sil_2–Bt_2 symplectites around Grt_2 against Crn. (f) Coarse Spl_2–Sil_2–Bt_2 symplectites developed as corona around Grt_2.

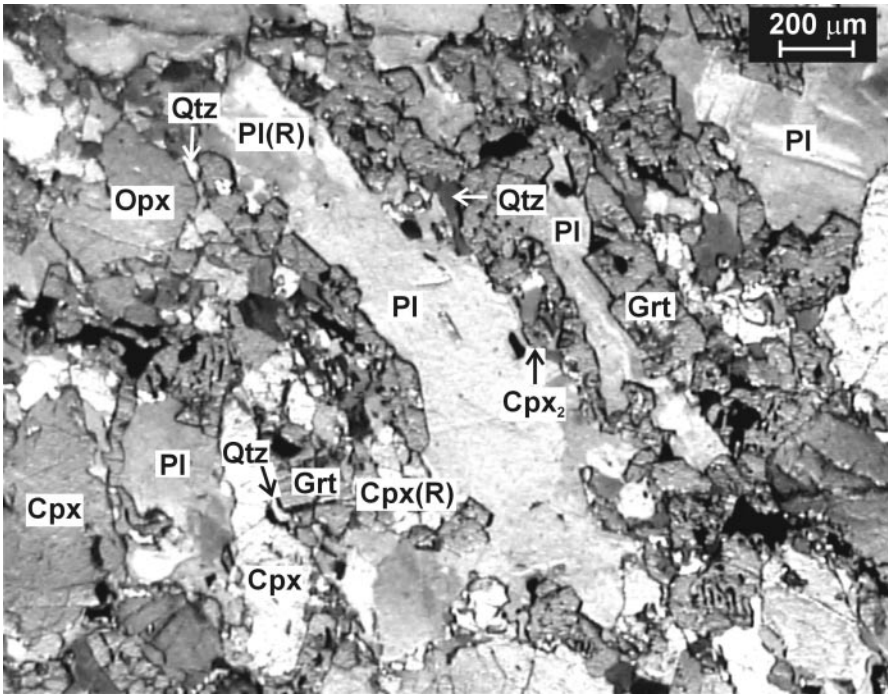

Fig. 7. Photomicrograph under partially crossed polars, showing the development of coronal Grt ± **C**px ± Qtz symplectites around megacrystic Opx, Cpx and Pl in mafic dyke, Md_1. The coronal occurrence of garnet around flattened Pl and also around recrystallized aggregates of Pl [Pl(R)] and Cpx [Cpx(R)] suggests that garnet in the mafic dyke has overgrown a strong deformation fabric, BS_3.

Mafic dyke$_1$

In the metamorphosed mafic dyke, Md_1, BD_3 has produced a flattened fabric, defined by elongate magmatic pyroxenes and plagioclase (Fig. 7). Coronal garnet ± quartz ± clinopyroxene-bearing symplectites occur around flattened and recrystallized grains of orthopyroxene, clinopyroxene, plagioclase and also ilmenite (Fig. 7).

MINERAL CHEMISTRY

The chemical compositions of the coexisting mineral phases in samples of felsic granulite, aluminous granulite and Md_1 were determined using a CAMECA SX-51 electron microprobe at the laboratory of the Geological Survey of India at Faridabad, and a Cameca Camebax Microbeam Electron Microprobe at the University of Bonn, Germany. The operating conditions for both the instruments were set as 1 μm beam diameter, 15 kV accelerating voltage and 12 nA specimen current. The PAP correction scheme was used. Natural and synthetic minerals were used as standards. Representative mineral compositions are given in Tables 2–5. Mineral analyses along compositional profiles are not given here. X-ray element mapping of selected textural sites in one sample was carried out using a Jeol Superprobe at the University of Cologne, Germany. The operating conditions were set as 20 kV accelerating voltage and 40 nA specimen current.

Garnet

Felsic granulite

Representative chemical analyses are given in Table 2. The cores of garnet$_1$ show large inter-sample variation in composition from $Prp_{31}Grs_{06}Alm_{62}Sps_{01}$ to $Prp_{35-36}Grs_{03-04}Alm_{60}Sps_{01}$ (Fig. 8a). The lowest pyrope content in garnet$_1$ is noted in sample B223A(2). In the same sample, the core of garnet$_1$, which is mantled by orthopyroxene$_2$–plagioclase$_2$ symplectite (Figs 4 and 5a), and smaller garnets occurring as relicts in the symplectite haloes (Fig. 5a) record even lower pyrope contents (Fig. 8a). By contrast, garnet$_2$ overgrowth on garnet$_1$ is enriched in grossular and depleted in pyrope ($Prp_{23}Grs_{11}Alm_{65}Sps_{01}$ to $Prp_{28}Grs_{09}Alm_{62}Sps_{01}$) (Fig. 8a). The highest grossular content is noted in garnet$_2$ that has overgrown the recrystallized plagioclase grains in the matrix (Fig. 5c) (Sample No. B223A(2), Anal. No. A-36).

X-ray element mapping of garnet$_1$ in Fig. 5a shows that a large part of porphyroblastic garnet$_1$ is compositionally homogeneous with respect to Mg and Fe (Fig. 9a and b). There is, however, a sharp increase in Ca all along the rim of garnet$_1$ at the contact with garnet$_2$ and also locally

Table 2: Representative electron microprobe analyses of garnet in felsic granulite, aluminous granulite and mafic dyke$_1$

	Felsic granulite							Aluminous granulite										Mafic dyke$_1$		
Sample no:	B62A(1)	B223A(2)					B220A(1)	B220D(1)			B29(1)						B220D(5)		B12		
Site no:	A-29	C-2	C-18	C-35	A-36	C-70	B-19	B-22	A-13	B-3	A-24	A-17	A-8	A-7	F-28	A-2	B-10	B-19	A-5	A-6	B-8
Textural site:	G_1(C)	G_1(C)	G_1(C)	G_2	G_2(C)	G_2	G_1(C)	G_2(C)	Grt_2^Spl_1	G_2 (Re)	G_1(C)	G_1(R)	G_2(C)	Grt_2^Spl_1	Grt_2^Spl_1	G_2(R)	G_1(C)	G_2(C)	COR	COR	COR
SiO_2	39·00	38·49	38·95	37·94	38·14	38·37	38·94	39·54	38·62	37·79	39·27	38·01	39·01	38·98	38·21	38·78	38·94	38·51	38·20	38·34	38·69
TiO_2	0·04	0·04	0·04	0·03	0·03	0·04	0·04	0·03	0·01	0·03	—	0·02	0·03	—	0·01	0·01	—	—	0·03	0·03	0·04
Al_2O_3	21·96	21·80	21·78	21·87	20·97	21·91	22·31	21·77	21·21	22·03	22·25	21·95	22·27	22·28	21·83	21·97	22·49	22·50	21·32	21·61	21·89
Cr_2O_3	—	0·09	0·08	0·18	0·27	0·07	0·10	0·03	—	0·01	0·03	0·03	—	0·01	0·00	—	0·05	—	—	—	0·04
FeO	28·09	29·86	30·11	29·04	30·11	30·42	28·12	28·81	30·13	32·79	27·96	29·67	26·53	29·03	31·29	31·04	26·36	26·78	27·25	27·14	27·13
MnO	0·62	0·32	0·51	0·45	0·57	0·49	0·38	0·38	0·37	0·36	0·53	0·46	0·42	0·34	0·44	0·50	0·45	0·38	0·60	0·50	0·54
MgO	9·12	8·10	7·68	7·29	5·93	6·16	9·43	9·65	8·73	6·33	8·98	7·80	10·44	8·71	6·97	7·54	11·07	9·82	5·18	5·11	5·28
CaO	1·33	1·88	2·04	3·27	3·90	3·85	1·24	0·76	0·85	1·05	1·14	1·44	1·03	1·34	1·43	1·31	1·15	0·86	7·74	8·08	7·18
Total	100·16	100·58	101·19	100·07	99·92	101·31	100·56	100·97	99·92	100·39	100·16	100·18	99·73	100·69	100·18	101·15	100·51	98·85	100·32	100·81	100·79
Oxygens	12	12	12	12	12	12	12	12	12	12	12	12	12	12	12	12	12	12	12	12	12
Si	3·001	2·972	2·997	2·949	2·998	2·967	2·979	3·016	2·998	2·962	3·014	2·972	2·987	2·992	2·985	2·991	2·949	2·980	2·976	2·974	2·997
Ti	0·002	0·002	0·002	0·002	0·002	0·002	0·002	0·002	0·001	0·002	—	0·001	0·002	—	0·001	0·001	—	—	0·002	0·002	0·002
Al	1·992	1·984	1·976	2·004	1·943	1·998	2·012	1·958	1·941	2·035	2·013	2·024	2·010	2·016	2·010	1·998	2·008	2·052	1·958	1·976	1·999
Cr^{3+}	—	0·005	0·005	0·011	0·017	0·004	0·006	0·002	—	0·001	0·002	0·002	—	0·001	0·000	—	0·003	—	—	—	0·002
Fe	1·808	1·928	1·937	1·887	1·980	1·967	1·799	1·838	1·956	2·149	1·795	1·940	1·698	1·863	2·044	2·002	1·669	1·733	1·776	1·779	1·758
Mn	0·040	0·021	0·033	0·030	0·038	0·032	0·025	0·025	0·024	0·024	0·034	0·030	0·027	0·022	0·029	0·033	0·029	0·025	0·040	0·033	0·035
Mg	1·046	0·932	0·881	0·844	0·695	0·710	1·075	1·097	1·010	0·739	1·027	0·909	1·191	0·996	0·811	0·867	1·249	1·132	0·602	0·591	0·610
Ca	0·110	0·156	0·168	0·273	0·329	0·319	0·102	0·062	0·071	0·088	0·094	0·121	0·085	0·110	0·120	0·108	0·093	0·071	0·647	0·672	0·597
Sum	7·999	8·000	7·999	8·000	8·002	7·999	8·000	8·000	8·001	8·000	7·979	7·999	8·000	8·000	8·000	8·000	8·000	7·993	8·001	8·027	8·000
X_{Prp}	0·348	0·307	0·292	0·278	0·228	0·234	0·358	0·363	0·330	0·247	0·348	0·303	0·397	0·333	0·270	0·288	0·411	0·382	0·196	0·192	0·203
X_{Alm}	0·602	0·635	0·641	0·622	0·651	0·650	0·600	0·608	0·639	0·716	0·608	0·647	0·566	0·623	0·680	0·665	0·549	0·585	0·580	0·579	0·586
X_{Sps}	0·013	0·007	0·011	0·010	0·013	0·011	0·008	0·008	0·008	0·008	0·012	0·010	0·009	0·007	0·010	0·011	0·009	0·009	0·013	0·011	0·012
X_{Grs}	0·037	0·051	0·056	0·090	0·108	0·105	0·034	0·021	0·023	0·029	0·032	0·040	0·028	0·037	0·040	0·036	0·031	0·024	0·211	0·218	0·199

G_1(C), G_1(R): core—rim of porphyroblastic Grt_1; G_2: second-generation Grt in felsic and aluminous granulite; Anal. No. C-2: core of Grt_1 away from Opx_2—Pl_2 symplectite; Anal. No. C-18: core of Grt_1 mantled by Opx_2—Pl_2 symplectite; Grt_2^Spl_1: garnet$_2$ against included spinel$_1$; G_2(Re): Grt_2 relict within Spl_2—Sil_2—Bt_2 symplectites; COR: coronal Grt in Md_1.

Table 3: Representative electron microprobe analyses of pyroxenes

	Felsic granulite										Mafic dyke$_1$					
Sample no:	B62A(1)	B223A(2)								B220A(1)	B12					
	Opx	Opx	Opx	Opx	Opx	Opx	Opx	Opx	Opx	Opx	Opx	Opx	Cpx	Cpx	Cpx	Cpx
Site no:	A-5	A-27	A-25	A-26	A-14	A-15	C-64	C-68	C-69	B-3	B-13	B-16	A-20	A-16	B-14	B-7
Textural site:	P(C)	P(C)	S(C)	S(R)	S(C)	S(C)	S(R)	S(C)	S(R)	P(C)	M(C)	M(R)	M(C)	M(R)	S	S
SiO_2	50·24	51·18	51·47	51·59	51·90	51·19	52·05	51·93	52·37	49·63	52·18	52·48	52·88	51·25	53·55	53·32
TiO_2	0·08	0·10	0·07	0·06	0·06	0·07	0·05	0·08	0·06	0·07	0·05	0·04	0·15	0·11	0·12	0·11
Al_2O_3	4·31	1·41	2·22	1·57	2·00	2·04	1·93	1·55	1·43	5·63	0·89	0·67	1·69	1·49	1·33	1·27
Cr_2O_3	0·17	0·07	0·03	0·04	0·12	0·05	0·13	0·11	0·07	0·11	0·00	0·00	0·06	0·03	0·03	0·03
FeO	24·73	28·20	25·81	26·96	25·67	26·27	26·10	26·58	27·17	23·48	27·00	27·32	9·83	10·15	9·13	8·04
MnO	0·26	0·18	0·13	0·12	0·16	0·19	0·14	0·12	0·13	0·08	0·21	0·18	0·08	0·06	0·07	0·07
MgO	19·32	18·15	19·76	19·03	19·39	19·48	20·56	20·42	20·37	20·36	18·89	19·10	13·10	13·10	13·57	13·85
CaO	0·12	0·35	0·26	0·25	0·41	0·27	0·26	0·30	0·27	0·11	0·59	0·36	22·20	22·34	22·56	22·84
Na_2O	0·01	0·02	0·01	—	0·02	0·02	0·04	—	—	0·02	0·01	0·00	0·49	0·53	0·40	0·38
K_2O	0·00	0·01	—	—	0·13	—	0·05	—	0·01	0·01	0·00	0·01	0·01	0·00	0·00	0·01
Total	99·24	99·67	99·76	99·62	99·86	99·58	101·31	101·09	101·88	99·50	99·82	100·16	100·49	99·06	100·76	99·92
Oxygens	6	6	6	6	6	6	6	6	6	6	6	6	6	6	6	6
Si	1·905	1·965	1·949	1·967	1·963	1·947	1·937	1·941	1·946	1·862	1·987	1·992	1·966	1·931	1·982	1·983
Ti	0·002	0·003	0·002	0·002	0·002	0·002	0·001	0·002	0·002	0·002	0·001	0·001	0·004	0·003	0·003	0·003
Al (IV)	0·095	0·035	0·051	0·033	0·037	0·053	0·063	0·059	0·054	0·138	0·013	0·008	0·034	0·066	0·018	0·017
Al (VI)	0·098	0·029	0·048	0·038	0·052	0·038	0·022	0·009	0·009	0·111	0·027	0·022	0·040	0·000	0·040	0·039
Cr^{3+}	0·005	0·002	0·001	0·001	0·004	0·002	0·004	0·003	0·002	0·003	0·000	0·000	0·002	0·001	0·001	0·001
Fe^{3+}	0·000	0·000	—	—	—	0·011	0·040	0·041	0·041	0·022	0·000	0·000	0·020	0·103	0·000	0·000
Fe^{2+}	0·784	0·905	0·817	0·860	0·812	0·825	0·773	0·790	0·804	0·715	0·860	0·867	0·286	0·217	0·282	0·250
Mn	0·008	0·006	0·004	0·004	0·005	0·006	0·004	0·004	0·004	0·003	0·007	0·006	0·003	0·002	0·002	0·002
Mg	1·092	1·039	1·115	1·081	1·093	1·104	1·140	1·138	1·128	1·138	1·072	1·081	0·726	0·736	0·748	0·768
Ca	0·005	0·014	0·011	0·010	0·017	0·011	0·010	0·012	0·011	0·004	0·024	0·015	0·884	0·902	0·894	0·910
Na	0·001	0·001	0·001	—	0·001	0·001	0·003	—	—	0·001	0·001	0·000	0·035	0·039	0·029	0·027
K	0·000	0·000	—	—	0·006	—	0·002	—	—	—	0·000	0·000	0·000	0·000	0·000	0·000
Sum	3·995	3·999	3·999	3·996	3·992	4·000	3·999	3·999	4·001	3·999	3·992	3·992	4·000	4·000	3·999	4·000
X_{Mg}	0·582	0·535	0·577	0·557	0·574	0·572	0·596	0·590	0·584	0·614	0·555	0·555	0·717	0·772	0·726	0·754

P(C): core of porphyroblastic Opx$_1$; S(C), S(R): core and rim of symplectitic Opx$_2$; M(C), M(R): core—rim of megacrystic pyroxenes; S: symplectitic Cpx in Md$_1$.

inside garnet$_1$, where the symplectic plagioclase$_2$ advanced well within the interior (Fig. 9c).

Compositional profiling of garnet along a traverse A–B (Fig. 9d and e) across two garnet grains is shown in Fig. 10a. Both the garnet grains show progressive rimward enrichment in grossular and concomitant depletion in pyrope and almandine contents. The high-grossular and low-pyrope content of garnet$_2$ immediately right of the contact is obvious. Such a compositional variation across a natural garnet–garnet couple, involving two end-member garnet$_1$ and garnet$_2$ compositions, can be explained by the operation of a very complex Ca–Mg–Fe diffusion, that provides clues regarding the time-scales of orogenic processes (Ganguly *et al.*, 1996). This aspect will be treated in a separate publication.

Aluminous granulites

Cores of porphyroblastic garnet$_1$ and coarse garnet$_2$ are uniformly pyrope-rich and grossular-poor ($Prp_{35–41}Grs_{03–02}Alm_{55–61}Sps_{01}$) (Table 2). Rims of garnet$_1$ are depleted in pyrope and enriched in almandine ($Prp_{25–30}Grs_{04}Alm_{65–72}Sps_{01}$). A similar composition is noted for garnet$_2$ in contact with spinel$_2$–sillimanite$_2$–biotite$_2$

Table 4: Representative electron microprobe analyses of feldspars

	Felsic granulite								Aluminous granulite								Mafic dyke$_1$		
Sample no:	B62A(1)	B220A(1)	B223A(2)						B220D(1)	B29(1)			B220D(5)				B12		
	Pl	Pl	Pl	Pl	Pl	Pl	Afs*	Tfs	Pl	Pl	Pl	Pl	Tfs	Tfs	Pl	Pl	Pl	Pl	Pl
Site no:	A-20	B-24	C-54	A-10	A-19-	B-3	C-4	R(3)	A-15	C-1	A-15	A-16	R(1)	R(2)	B-20	B-14	B-3	B-6	B-5
Textural site:	P(C)	P(C)	S(C)	S(R)	Cor^Per			M	I^Grt$_2$	I^Sil$_2$	M(C)	M(R)	I^Grt$_1$	M	I^Spr	I^Grt$_2$	MG(C)	MG(R)	MG(E)
SiO_2	60·94	61·96	59·91	60·18	60·60	59·31	63·24	60·29	62·57	59·92	61·04	58·86	64·52	64·06	63·75	63·39	53·45	50·39	58·64
TiO_2	0·04	—	0·01	—	0·03	—	0·01	—	0·01	0·01	0·01	0·07	—	—	—	0·01	—	—	—
Al_2O_3	24·10	24·16	24·84	24·78	24·77	26·50	18·91	24·60	22·48	25·49	25·25	25·14	20·13	20·20	22·91	23·41	30·48	32·46	27·18
Cr_2O_3	0·03	—	—	—	—	—	—	—	—	0·02	—	—	—	—	0·01	—	—	—	—
FeO	—	0·02	0·04	0·84	0·40	0·03	0·03	0·03	0·46	0·07	—	0·22	0·03	0·02	0·48	0·58	0·05	0·04	0·04
MnO	0·04	—	0·03	—	—	—	—	—	—	0·02	0·01	—	0·01	—	0·01	0·01	—	0·03	0·07
MgO	0·01	0·01	—	0·39	0·23	—	0·02	0·01	0·01	—	—	0·02	—	—	0·03	0·03	—	—	0·01
CaO	6·16	5·40	7·40	6·22	6·03	7·64	0·04	5·74	4·20	6·68	6·61	5·77	1·27	1·26	3·52	4·07	12·51	14·97	8·71
Na_2O	8·25	8·66	7·84	7·94	8·05	7·40	0·95	5·79	9·32	8·24	8·09	8·71	5·40	5·17	9·77	9·65	4·56	3·07	6·69
K_2O	0·26	0·26	0·18	0·14	0·17	0·21	15·10	3·93	0·10	0·12	0·22	0·19	8·35	9·14	0·08	0·14	0·11	0·07	0·20
Total	99·83	100·47	100·25	100·49	100·28	101·09	98·30	100·39	99·15	100·57	101·23	98·98	99·71	99·85	100·56	101·29	101·16	101·03	101·54
(O)	8	8	8	8	8	8	8	8	8	8	8	8	8	8	8	8	8	8	8
Si	2·717	2·738	2·670	2·671	2·689	2·621	2·965	2·703	2·795	2·659	2·686	2·655	2·923	2·911	2·803	2·774	2·392	2·273	2·586
Ti	0·001	—	—	—	0·001	—	—	—	—	—	—	0·002	—	—	—	—	—	—	—
Al	1·267	1·259	1·305	1·296	1·296	1·381	1·045	1·300	1·184	1·333	1·310	1·337	1·075	1·082	1·187	1·208	1·608	1·727	1·413
Cr^{3+}	0·001	—	—	—	—	—	—	—	—	0·001	—	—	—	—	—	—	—	—	—
Fe^{3+}	—	0·001	0·001	0·031	0·015	0·001	0·001	0·001	0·017	0·003	—	0·008	0·001	0·001	0·018	0·021	0·002	0·002	0·001
Mn	0·002	—	0·001	—	—	—	—	—	—	0·001	—	—	—	—	—	—	—	0·001	0·003
Mg	0·001	0·001	—	0·026	0·015	—	0·001	0·001	0·001	—	—	0·001	—	—	0·002	0·002	—	—	0·001
Ca	0·294	0·256	0·353	0·296	0·287	0·362	0·002	0·276	0·201	0·318	0·312	0·279	0·062	0·061	0·166	0·191	0·600	0·724	0·412
Na	0·713	0·742	0·678	0·683	0·693	0·634	0·086	0·503	0·807	0·709	0·690	0·762	0·474	0·455	0·833	0·819	0·396	0·269	0·572
K	0·015	0·015	0·010	0·008	0·010	0·012	0·904	0·225	0·006	0·007	0·012	0·011	0·483	0·530	0·004	0·008	0·006	0·004	0·011
Sum	5·011	5·012	5·018	5·011	5·006	5·011	5·004	5·009	5·011	5·031	5·010	5·055	5·018	5·040	5·013	5·023	5·004	5·000	4·999
X_K	0·015	0·015	0·010	0·008	0·010	0·012	0·911	0·224	0·006	0·007	0·012	0·010	0·474	0·507	0·004	0·008	0·006	0·004	0·011
X_{Na}	0·698	0·732	0·651	0·692	0·700	0·629	0·087	0·501	0·796	0·686	0·680	0·724	0·465	0·435	0·831	0·805	0·395	0·270	0·575
X_{Ca}	0·288	0·253	0·339	0·300	0·290	0·359	0·002	0·275	0·198	0·308	0·308	0·265	0·061	0·058	0·166	0·188	0·599	0·726	0·414

Afs*: alkali feldspar; Tfs: ternary feldspar; P(C): core of porphyroblast; S(C), S(R): symplectite core—rim; Cor^Per: corona around perthite against Grt$_1$; I^Grt$_2$: included within Grt$_2$; I^Spr: included within Spr; I^Sil$_2$: included within Sil$_2$; M(C), M(R): core—rim of matrix Pl; MG(C), MG(R), MG(E): megacrystic core—rim-edge; Anal. Nos B-3, C-4: coexisting plagioclase host and alkali feldspar exsolution lamellae in mesoantiperthites; R(1), R(2): reintegrated composition of mesoperthites included within Grt$_1$ and in the matrix, respectively; R(3): reintegrated composition of mesoantiperthites.

Table 5: Representative electron microprobe analyses of biotite, spinel and sapphirine of felsic granulite and aluminous granulite

	Felsic granulite		Aluminous granulite												
Sample no:	B223A(2)		B220D(1)						B220D(5)			B29(1)			
	Bt_1	Bt_1	Spl_1	Spl_1	Spl_2	Spl_2	Spl_2	Bt_1	Spl_1	Spl_1	Spr	Spl_1	Spl_1	Spl_2	Bt_1
Site no:	A-23	B-28	A-9	A-12	A-1	A-8	A-20	A-10	B-15	B-1	B-1	F-29	B-4	B-3	F-2
Textural site:	I^Grt_1	I^Grt_1	I^Grt_2	I^Grt_2	S	S	S	I^Grt_1	I^Grt_2	I^Per	I^Grt_2	I^Grt_2	I^Grt_2	S	I^Grt_1
SiO_2	37·75	37·97	0·06	0·06	0·04	0·05	0·06	37·73	0·02	0·05	13·82	0·04	0·03	0·05	38·86
TiO_2	4·01	3·63	0·01	—	—	0·02	—	3·76	—	—	0·06	0·00	—	0·01	4·89
Al_2O_3	15·05	15·37	61·56	60·83	59·30	57·98	56·07	16·72	62·51	59·19	61·31	59·57	60·31	56·99	16·67
Cr_2O_3	0·11	0·12	0·60	0·49	1·29	1·73	2·82	0·13	0·56	0·93	0·17	1·29	0·73	2·14	0·29
FeO	10·88	10·96	21·92	22·93	25·44	26·14	26·20	7·97	21·31	29·41	9·58	21·30	20·80	28·13	7·73
MnO	0·01	0·02	0·05	—	0·01	0·03	—	0·02	0·02	0·02	—	0·00	0·06	0·03	0·15
MgO	16·84	16·56	12·14	11·24	7·07	6·27	7·17	18·75	10·58	5·46	14·70	7·73	10·50	7·29	17·99
CaO	0·01	0·02	—	—	—	—	—	0·02	0·01	0·04	0·01	0·00	—	—	0·01
Na_2O	0·10	0·07	—	—	—	—	—	0·11	—	—	0·02	0·16	—	—	0·11
K_2O	9·32	10·03	—	—	—	—	—	10·16	—	—	—	0·01	—	—	8·86
BaO	0·05	—	—	—	—	—	—	0·65	—	—	—	0·21	—	—	—
ZnO	0·02	—	2·90	2·99	5·03	6·63	4·66	0·03	3·54	4·07	—	7·91	5·92	3·04	0·12
Total	94·15	94·75	99·24	98·54	98·18	98·85	96·98	96·05	98·55	99·17	99·67	98·22	98·35	97·68	95·68
Oxygens	22	22	4	4	4	4	4	22	4	4	20	4	4	4	22
Si	5·590	5·604	0·002	0·002	0·001	0·002	0·002	5·448	0·001	0·001	1·662	0·001	0·001	0·001	5·546
Ti	0·447	0·402	—	—	—	—	—	0·408	—	—	0·005	0·000	—	—	0·525
Al	2·627	2·674	1·949	1·950	1·969	1·936	1·899	2·846	1·999	1·970	8·693	1·973	1·954	1·908	2·804
Cr^{3+}	0·013	0·013	0·013	0·011	0·029	0·039	0·064	0·015	0·012	0·021	0·016	0·029	0·016	0·048	0·033
Fe^{3+}	—	—	0·035	0·036	—	0·021	0·034	—	—	—	—	—	0·029	0·041	—
Fe^{2+}	1·347	1·353	0·457	0·486	0·599	0·598	0·596	0·963	0·483	0·695	0·964	0·501	0·449	0·628	0·923
Mn	0·001	0·002	0·001	—	—	0·001	—	0·002	—	—	—	0·000	0·001	0·001	0·018
Mg	3·718	3·644	0·486	0·456	0·297	0·265	0·307	4·036	0·428	0·230	2·635	0·324	0·430	0·309	3·827
Ca	0·002	0·003	—	—	—	—	—	0·003	—	0·001	0·001	0·000	—	—	0·002
Na	0·029	0·021	—	—	—	—	—	0·031	—	—	0·005	0·009	—	—	0·030
K	1·761	1·889	—	—	—	—	—	1·872	—	—	—	0·000	—	—	1·613
Ba	0·003	—	—	—	—	—	—	0·037	—	—	—	0·002	—	—	—
Zn	0·002	—	0·057	0·060	0·105	0·139	0·099	0·003	0·071	0·085	—	0·164	0·120	0·064	0·013
Sum	15·540	15·605	3·000	3·001	3·000	3·001	3·001	15·664	2·994	3·003	13·981	3·003	3·000	3·000	15·334
X_{Mg}	0·734	0·729	0·515	0·484	0·331	0·307	0·340	0·807	0·470	0·249	0·732	0·393	0·489	0·330	0·806

I^Grt_1: inclusion within Grt porphyroblast; I^Grt_2: inclusion within second-generation Grt; I^Per: inclusion within perthites; S: symplectites; $X_{Mg} = Mg/(Mg + Fe^{2+})$.

symplectite. $Garnet_2$ in contact with included $spinel_1$ shows Fe–Mg compositional variation depending on its grain size and that of the associated $spinel_1$. Coarse $garnet_2$ (grain diameter in the range of 1–1·7 mm) in contact with small $spinel_1$ is depleted in X_{Mg} ($X_{Mg} = Mg/Mg + Fe^{2+}$) by 0·03–0·06 units, relative to $garnet_2$ cores away from $spinel_1$ (Fig. 8b). Smaller $garnet_2$ (grain diameter in the range of 0·3–0·4 mm) in contact with coarser $spinel_1$ (in Fig. 6c) shows even larger depletion in X_{Mg} (by 0·09 unit) (Fig. 10b).

Mafic dyke1

Coronal garnet in Md_1 is compositionally homogeneous with uniformly high almandine and grossular and

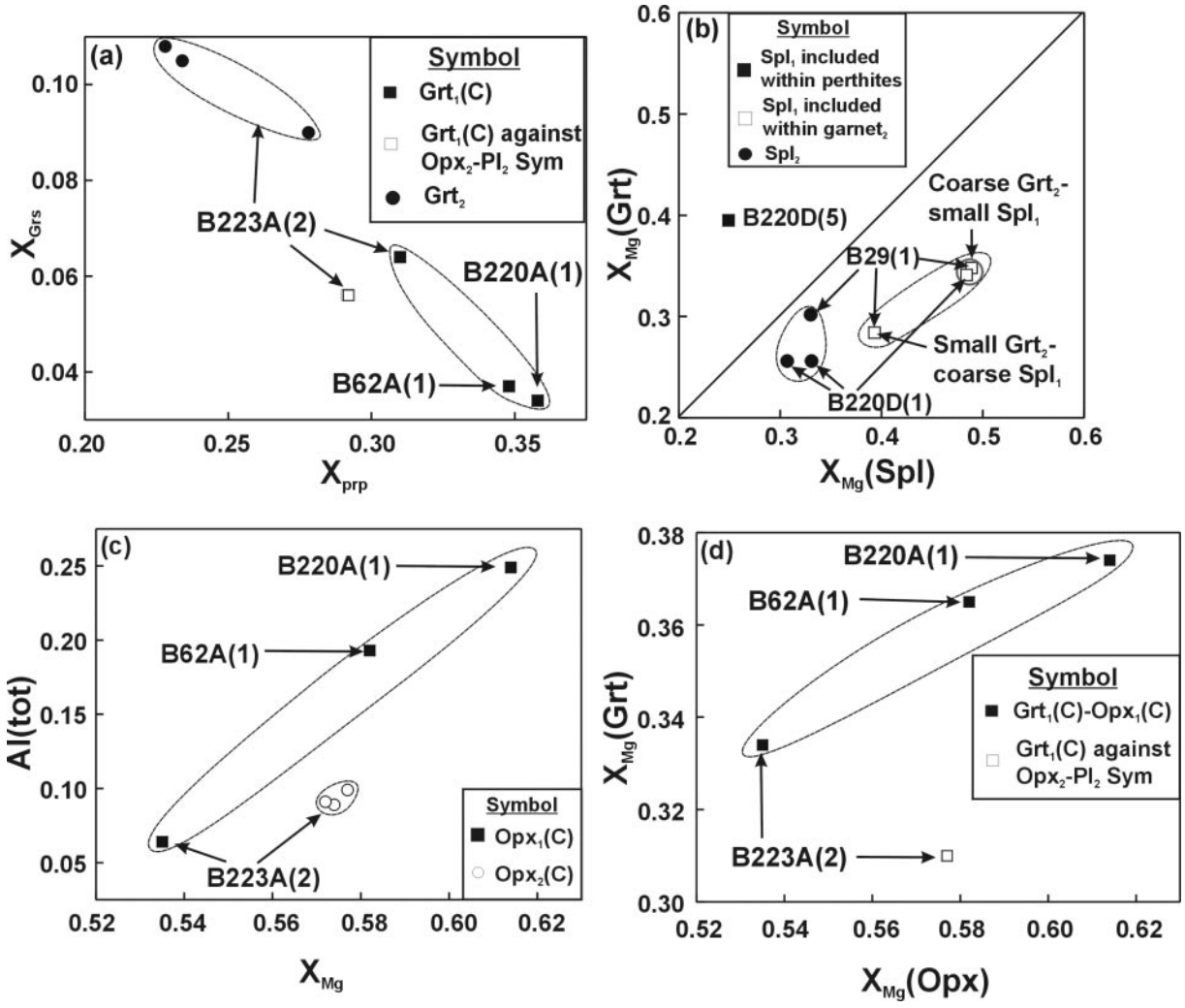

Fig. 8. Compositional variation in garnet (a), orthopyroxene (c) and coexisting garnet and orthopyroxene (d) from felsic granulite and in coexisting spinel and garnet from aluminous granulite (b).

relatively lower pyrope contents ($Prp_{19–20}Grs_{20–22}Alm_{58–59}Sps_{01}$) (Table 2).

Orthopyroxene–clinopyroxene

Felsic granulite

Cores of porphyroblastic orthopyroxene$_1$ show large inter-sample variation in X_{Mg} (0·54–0·61) and Al_{tot} ($Al_{tot} = Al^{IV} + Al^{VI}$) (0·06–0·25) (Table 3). The sample with the highest X_{Mg} also records the highest alumina in orthopyroxene$_1$ (Fig. 8c). In sample B223A(2), the coarse orthopyroxene$_2$ cores are more magnesian (X_{Mg} = 0·57–0·58) and aluminous (Al_{tot} = 0·09–0·10) relative to orthopyroxene$_1$ cores (X_{Mg} = 0·54, Al_{tot} = 0·06) (Fig. 8c). In general, orthopyroxene$_2$ has similar X_{Mg}, but shows variation in Al_{tot}-content (from 0·10 to 0·06). The latter varies with grain size (smaller grains at 0·06–0·07) and from core (0·10) to rim (0·07).

In Fig. 8d, the variation of X_{Mg} in cores of coexisting orthopyroxene$_1$ and garnet$_1$ is plotted; this shows positive covariation. The sample containing the most magnesian garnet is also characterized by the most magnesian, and also the most aluminous, orthopyroxene.

Mafic dyke$_1$

Megacrystic orthopyroxene is magnesian (X_{Mg} = 0·56) and low in alumina (Al_{tot} = 0·03–0·04) (Table 3). There is slight rimward fall in Al_{tot} contents (0·04 in core to 0·03 in rim). Megacrystic clinopyroxene in comparison is more aluminous (Al_{tot} = 0·06–0·07) and magnesian (X_{Mg} = 0·72–0·78). There is small rimward depletion in Al-content of clinopyroxene in contact with coronal

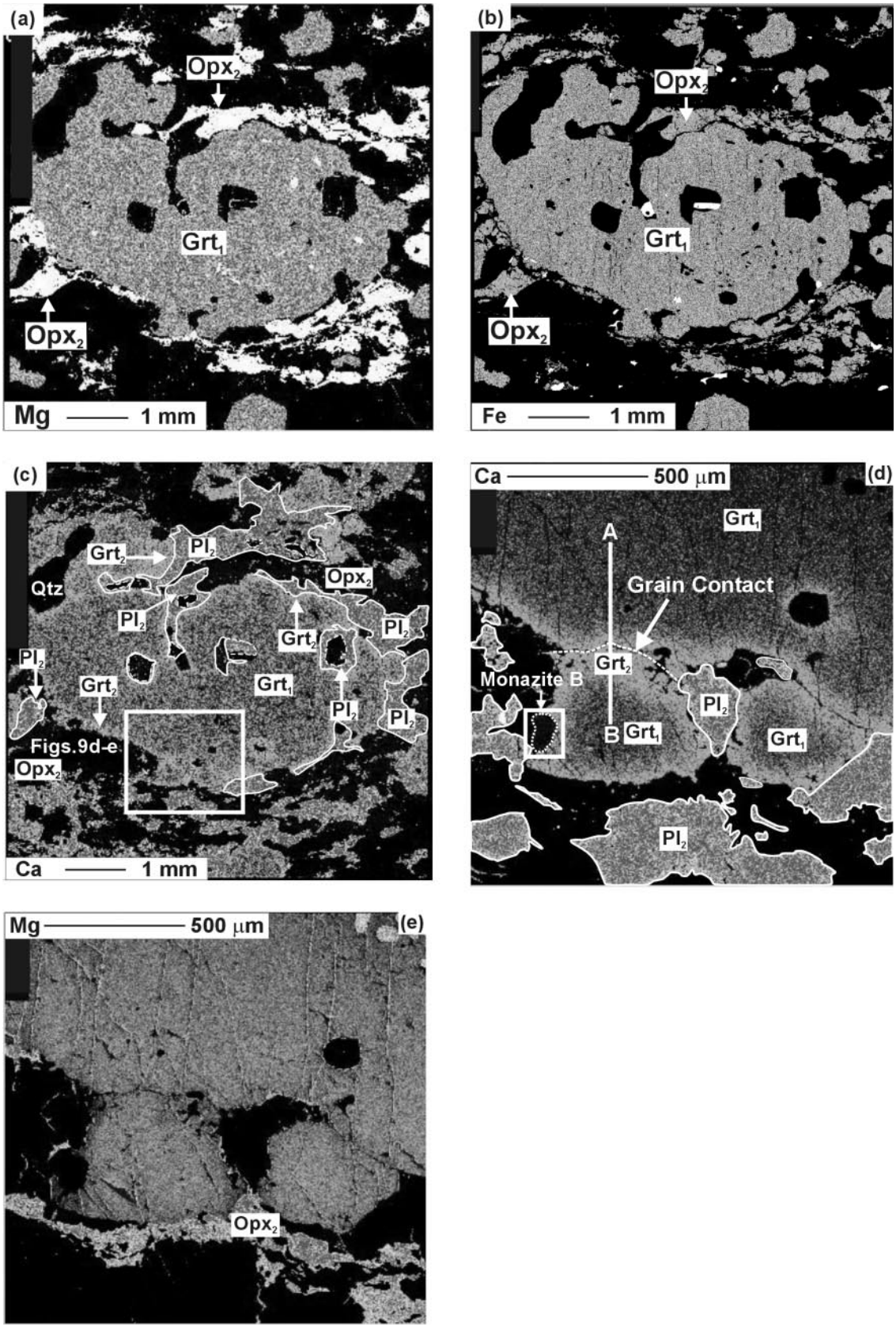

garnet. Coronal clinopyroxene is compositionally similar to that of megacrystic clinopyroxene rim.

Plagioclase

Felsic granulite

Cores of plagioclase$_1$ range in composition from An_{25} to An_{29}, whereas cores of plagioclase$_2$ are more calcic (An_{34}) (Table 4). The latter shows depletion in An-content towards the rims (An_{29}) against garnet$_2$. Reintegrated mesoantiperthite is of the composition $An_{27}Ab_{50}Or_{23}$ [Anal. No. R(3), Table 4].

Aluminous granulites

The composition of plagioclase varies in the range $An_{17–31}$.

Mafic dyke$_1$

Megacrystic plagioclase is reversely zoned, with X_{An} systematically increasing from An_{60} in the core to An_{73} in rim (Table 4); however, the An-content falls sharply (An_{41}) against coronal garnet.

Perthite

Aluminous granulites

Reintegration of mesoperthite composition was carried out with a broad beam (30 μm beam diameter). Regardless of its mode of occurrence, the pre-exsolution composition of the alkali feldspar is calculated as $Or_{47–51}Ab_{44–47}An_6$ [Anal. Nos R(1), R(2); Table 4].

Spinel and sapphirine

Aluminous granulites

In the aluminous granulites, spinel$_1$ included in garnet$_2$ and in mesoperthite in the leucocratic layers shows sharply different composition (Fig. 8b; Table 5). The latter is the most ferroan, with X_{Mg} value of ~0·25 [Sample No. B220D (5), Anal. No. B-1]. Irrespective of the sample, spinel$_1$ included within garnet$_2$ is always magnesian (X_{Mg} = 0·39–0·52) (Fig. 8b; see Table 5 also). A relatively ferroan composition is observed in coarser spinels (grain diameter in the range of 0·06–0·08 mm), whereas smaller spinels (grain diameter in the range of 0·02–0·03 mm) are the most magnesian (Fig. 8b). Spinel$_1$ contains 6–12 mol % gahnite. Spinel$_2$, on the other hand, has a slightly higher gahnite content (max. 14 mol %) and intermediate X_{Mg} (0·31–0·34).

Sapphirine in the aluminous granulite is compositionally between the 221 and 793 (molar $MgO:Al_2O_3:SiO_2$ ratio) end-members without any Fe^{3+} and is highly magnesian (X_{Mg} = 0·73) (Table 5).

Biotite

Felsic granulite

Included biotite in garnet$_1$ in the felsic granulite is titaniferous (TiO_2 = 3·63–4·01 wt %) and magnesian (X_{Mg} = 0·73) (Table 5).

Aluminous granulites

In the aluminous granulites, included biotite within garnet$_1$ is even more titaniferous (TiO_2 = 4·89 wt %) and magnesian (X_{Mg} = 0·81) (Table 5). Biotite contains 0·12 wt % ZnO.

Summary

The observed inter-sample chemical trends in the felsic granulites reflect original bulk compositional control on the progress of different mineral reactions involving garnet$_1$ and orthopyroxene$_1$. These reactions are likely to have buffered the mineral compositions under restricted range of P–T conditions of metamorphism (see Fitzsimons & Harley, 1994). By contrast, the intra-specimen compositional variation of garnet and orthopyroxene at near-fixed bulk composition [e.g. in sample B223A(2)] possibly indicates subsequent changes in P–T conditions of metamorphism.

In the aluminous granulites, both intra- and inter-sample compositional variations indicate a reversal of the Fe–Mg compositional relationship between spinel and garnet, even at the scale of a thin section, giving rise to the compositional relationship $X_{Mg}(Spl_1) > X_{Mg}(Grt_2)$ for the melanocratic layers and $X_{Mg}(Spl_1) < X_{Mg}(Grt_1)$ for the leucocratic layers. Such compositional reversals between garnet and spinel are known from both experimental and natural rock data (reviewed by Fitzsimons, 1996) and may result from bulk compositional variation, retrograde re-equilibration and pressure variations. In this study, the authors observe considerable Fe^{2+}–Mg exchange between coexisting garnet$_2$ and spinel$_1$, the extent of diffusion being largely controlled by the grain size of the exchanging phases. Based on this observation, it is predicted that the original spinel$_1$ was compositionally Fe-rich relative to the garnet. The authors,

Fig. 9. X-ray element maps of Grt$_1$ and adjoining Opx$_2$–Pl$_2$ symplectite domains of felsic granulite, shown in Fig. 4. In all the maps, brighter and darker shades indicate higher and lower concentration of the elements, respectively. (a) and (b) Mg- and Fe-maps, showing uniform distribution of these elements in Grt$_1$. (c) Ca-map shows conspicuous Ca-zoning all along the Grt$_1$ rim and locally inside Grt$_1$. The Ca-content increases specifically against symplectitic Pl$_2$. Note that the Pl$_2$ boundary is demarcated by white borders. The box represents details of Ca and Mg X-ray element maps shown in (d) and (e), respectively. (d) Details of Ca-element map of two Grt$_1$ grains in contact. Ca concentration increases radially outward towards grain contact. The highest Ca concentration is observed all along the Grt periphery coinciding with the location of Grt$_2$. Note that one boundary of the monazite Grain B is in direct contact with Grt$_2$. (e) In contrast, Mg-zoning is much weaker, with a minor fall in Mg concentration in Grt$_2$.

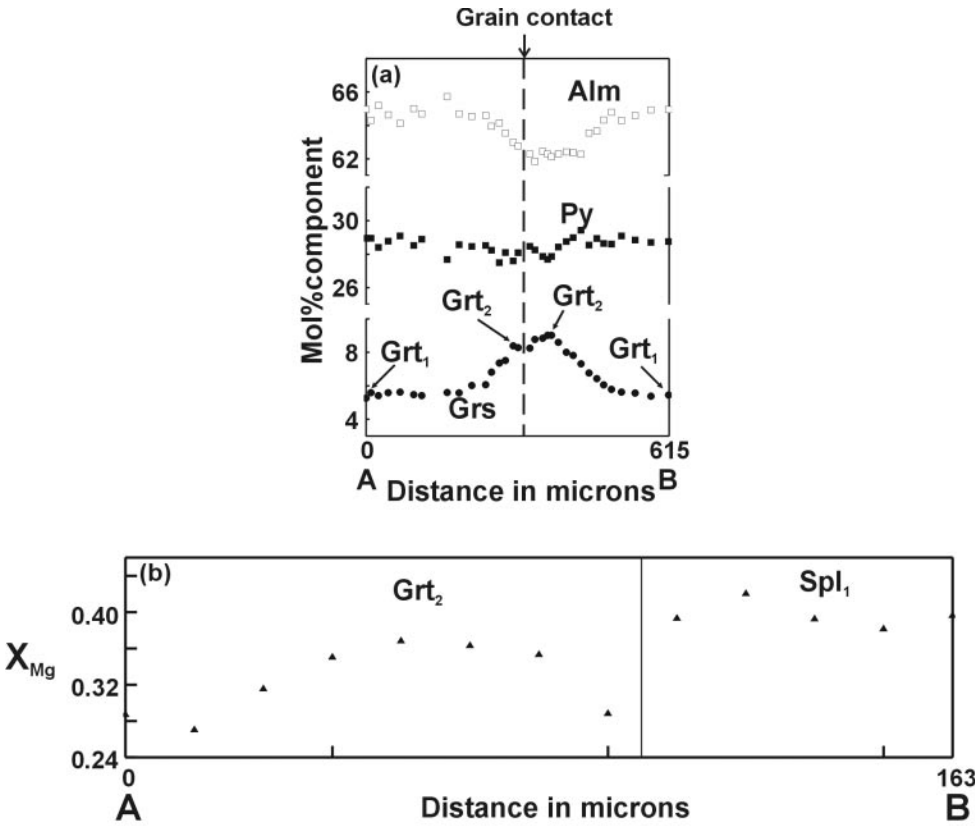

Fig. 10. (a) Compositional profile A–B across two Grt_1 grains in contact in felsic granulite. See Fig. 9d for location of the profile. (b) Compositional profile A–B in aluminous granulite, showing variation in X_{Mg} across coronal Grt_2 host and included Spl_1.

therefore, consider the X_{Mg} of the phases in the aluminous granulites to decrease in the following order: biotite–sapphirine–garnet–spinel. In the following section, they deduce the sequence of mineral reactions in the studied rocks using textural and compositional criteria. For the latter, compositions of the coexisting phases in the aluminous granulites are plotted in the SiO_2–FB–MB ternary system (projected from sillimanite, K-feldspar and melt) (Fig. 11a), where FB and MB represent Fe- and Mg-rich biotite (after McDade & Harley, 2001).

SEQUENCE OF MINERAL REACTIONS

The development of migmatitic banding, stabilization of the porphyroblastic $garnet_1$–$orthopyroxene_1$–perthite association, and the presence of biotite, plagioclase and quartz inclusions in $garnet_1$, are consistent with the progress of the dehydration–melting reaction

$$\text{biotite} + \text{plagioclase} + \text{quartz} = \text{garnet}_1 + \text{orthopyroxene}_1 + \text{perthite} + \text{L} \qquad \text{(R1)}$$

where L is melt phase.

The leucocratic layers in the gneiss can be considered to represent at least a part of the melt, with some peritectic phases (see, e.g. Moraes *et al.*, 2002). The reaction has been experimentally studied by many workers (Vielzeuf & Montel, 1994; Patiño Douce & Beard, 1995; Stevens *et al.*, 1997; Vielzeuf & Schmidt, 2001; Nair & Chacko, 2002). In the studied rocks, those with a high Ti-content in relict biotite, highly aluminous $orthopyroxene_1$ and pyrope-rich $garnet_1$ are consistent with ultrahigh temperatures of metamorphism ($T \geq 950°C$) *for reaction (R1) (Nair & Chacko, 2002).*

In the aluminous granulites, textural indications for the reaction leading to the stabilization of $garnet_1$ are not clear. However, by analogy with the felsic granulites, a similar biotite dehydration–melting reaction, involving additionally early sillimanite at high temperatures, can be predicted to account for the development of leucocratic layers with abundant mesoperthite and dark restitic layers. Abundant rutile in the aluminous granulites could be produced from the Ti liberated from biotite during melting (see Stevens *et al.*, 1997).

In the next stage of mineralogical evolution, an assemblage of $spinel_1$–sapphirine was formed in the aluminous granulites. In the total absence of cordierite, quartz and orthopyroxene, this assemblage can be produced by the

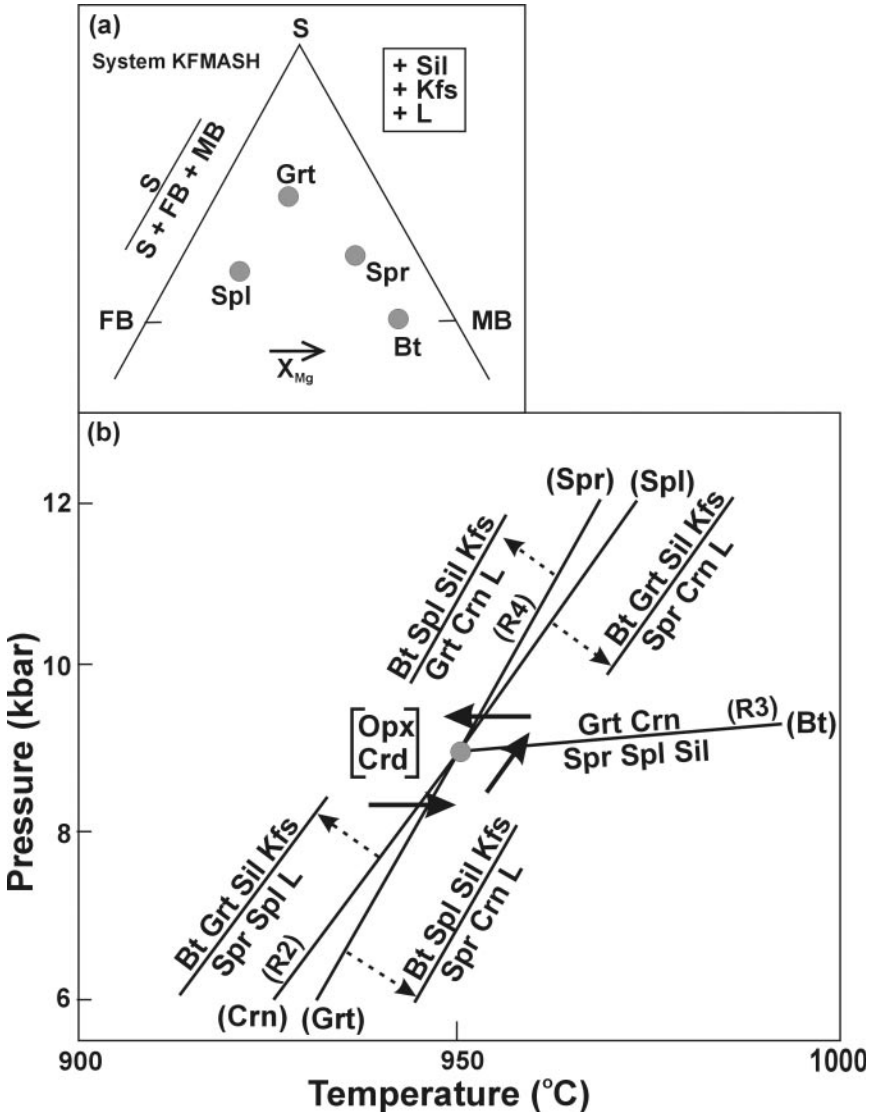

Fig. 11. (a) Chemographic relations of mineral phases in the S–FB–MB projection system in aluminous granulite. (b) Partial KFMASH petrogenetic grid, showing the stability field of Spr–Spl–Sil, Grt–Crn and Bt–Spl–Sil mineral assemblages in aluminous granulites. The continuous-line arrows point to the sequential operation of the mineral reactions (R2), (R3) and (R4), referred to in the text.

reaction

$$\text{garnet}_1 + \text{biotite} + \text{sillimanite}_1 \pm \text{K-feldspar} = \text{sapphirine} + \text{spinel}_1 + \text{L}. \quad \text{(R2)}$$

This reaction is analogous to the KFMASH univariant reaction (Opx, Crd, Qtz) earlier studied by McDade & Harley (2001). Compared with previous studies (e.g. Hensen & Harley, 1990; Mouri *et al.*, 1996), garnet and spinel switch positions in this reaction. Reaction (R2) has a high dP/dT slope, progresses to the right with increasing temperature, and is located at $T > 900°C$ (McDade & Harley, 2001). The compositional characteristics of biotite and spinel suggest that the gahnite content in spinel_1 was contributed by the reacting biotite. It is interesting to note that at this stage of mineral reaction history, quartz was removed from the matrix of the restite, obviously indicating progressive silica undersaturation.

Inclusions of sapphirine, sillimanite_1 and spinel_1 in garnet_2 (Fig. 6c and d) and the appearance of corundum containing inclusions of spinel_1 in the aluminous granulites and chemographic support (Fig. 11a) can be attributed to the simplified reaction

$$\text{sapphirine} + \text{sillimanite}_1 + \text{spinel}_1 = \text{garnet}_2 + \text{corundum}. \quad \text{(R3)}$$

This univariant reaction in the system FMAS is valid only if $X_{Mg}(Spl) < X_{Mg}(Grt)$ (see Hensen (1987) for the reverse compositional relation, $X_{Mg}(Spl) > X_{Mg}(Grt)$). The authors have used the ferruginous spinel composition in the leucocratic layers to deduce reaction (R3), assuming that the spinel occurring in contact with other ferromagnesian phases (such as garnet) in the restite re-equilibrated during the subsequent evolution of the rock. Reaction (R3) progresses to the right with cooling and/or loading and suggests further silica undersaturation. The rocks studied here, therefore, provide an evolutionary link between silica-saturated bulk composition and undersaturated ones, primarily brought about by melting and removal of silica (McDade & Harley, 2001).

Development of a coarse symplectite of spinel$_2$–sillimanite$_2$–biotite$_2$ between garnet$_2$ and corundum (Fig. 6e and f) is related to the simplified reaction

$$\text{garnet}_2 + \text{corundum} + \text{L} = \text{spinel}_2 + \text{sillimanite}_2 + \text{biotite}_2 \pm \text{K-feldspar}. \quad \text{(R4)}$$

Such melt–solid back reactions are commonly encountered during retrogression of UHT mineral assemblages (Moraes *et al.*, 2002), where the melt provides the water necessary to stabilize biotite. Even if sapphirine is absent, reaction (R4) implies reversal of the reaction (R3). Extensive exsolution in alkali feldspar in both the aluminous granulites and felsic granulites, producing mesoperthite, can be correlated with this cooling event.

An important observation related to the next stage of mineralogical evolution in the felsic granulite is that the orthopyroxene$_2$–plagioclase$_2$ symplectite at the margin of garnet$_1$ against quartz is aligned along BS_2 (Fig. 4). Orthopyroxene$_2$ and relict garnet$_1$ in the symplectites are Mg- and Al-rich, and ferroan, respectively, relative to orthopyroxene$_1$ and garnet$_1$ occurring away from the symplectites (Fig. 8d). These textural and compositional features attest to the reaction

$$\text{garnet}_1 + \text{quartz} = \text{orthopyroxene}_2 + \text{plagioclase}_2. \quad \text{(R5)}$$

Reaction (R5) progresses to the right due to decompression or heating. This aspect is further discussed in a later section.

Development of garnet$_2$–quartz symplectite at the expense of plagioclase$_2$ and orthopyroxene$_2$ as a metamorphic overgrowth on compositionally reset garnet$_1$ (Fig. 5d), and the compositional characteristics of the phases, signify backward movement of reaction (R5) in the felsic granulite in response to cooling, loading or a combination of both at a later stage. Since garnet$_2$ overgrew recrystallized plagioclase formed by deformation, BD_3 (Fig. 5c), the authors argue that garnet growth post-dated this deformation. Coeval with garnet$_2$ formation in the felsic granulite, coronal garnet appeared in Md_1 (Fig. 7) according to the reactions

$$\text{clinopyroxene} + \text{plagioclase} = \text{garnet} + \text{quartz} \quad \text{(R6)}$$

$$\text{orthopyroxene} + \text{plagioclase} = \text{garnet} + \text{clinopyroxene} + \text{quartz}. \quad \text{(R7)}$$

The sequence of mineral reactions in the studied rocks is, therefore, the product of (a) initial melting, leading to the production of porphyroblastic phases; (b) cooling; (c) heating/decompression; and (d) cooling/loading, producing various types of coronas–symplectites. For convenience of description, these are henceforth referred to as M_1 to M_4. The *P–T* conditions during each of the above stages of mineralogical evolution are evaluated in the following section based on thermobarometry calculations and petrogenetic grid considerations.

P–T CONDITIONS OF METAMORPHISM

Table 6 lists the results of thermobarometric computations using various methods. For the assemblage garnet–orthopyroxene–plagioclase–quartz in the felsic granulites, the authors employed the formulation of Pattison *et al.* (2003) that uses a convergence technique and accounts for late Fe–Mg exchange. For comparison, results obtained from the THERMOCALC program (ver. 3.1) (Holland & Powell, 1998) are given. Reintegrated mesoperthite compositions from the aluminous granulites, occurring both as inclusions within garnet$_1$ and in the matrix, when considered in the ternary feldspar diagram of Fuhrman & Lindsley (1988) gives a temperature of ~950°C (Fig. 12a). Using the core compositions of the porphyroblastic phases, *P–T* values of 9 ± 1 kbar, 900 ± 50°C were obtained for M_1 from the felsic granulites (Fig. 12b). Therefore, the peak metamorphic M_1 *P–T* conditions in the study area are taken as 9 kbar, 950°C. This implies that the granulites of the BBG domain join the select group of UHT metamorphosed rocks (Harley, 1998). Such high temperatures are consistent with the predicted biotite dehydration–melting reactions in both the felsic and aluminous granulites.

The *P–T* conditions and *P–T* path of evolution of the studied rocks can be further evaluated with the help of petrogenetic grids in the system KFMASH. The authors have constructed a partial petrogenetic grid around the invariant point [Crd, Opx] (Fig. 11b), using balanced univariant reactions (see Table 7) and the compositions of the studied phases. Melt composition is taken from Carrington & Harley (1995). The sequential progress of

Table 6: Results of geothermobarometry for the felsic granulite, aluminous granulite and mafic dyke$_1$

Sample no.	Site position	P_{Ref}	T_{GS}	T_{HP}	T_P	T_{Ref}	P_{FS} HP	P_{ES} HP	P_{DI} HP	P_{HD} HP	P_P	M
B62A(1)	Grt(A-29)–Opx(A-5)–Pl(A-20)	9·0			862	950	8·4	7·7			8·0	M_1
B220A(1)	Grt(B-19)–Opx(B-3)–Pl(B-24)	9·0			951	950	9·3	7·5			10·0	M_1
B220D(5)	Grt(B-19)–Spl(B-1)	9·0	910									M_2
B220D(1)	Grt(B-3)–Spl(A-8)	9·0	810									M_2
	Grt(B-3)–Spl(A-1)	9·0	820									M_2
B29(1)	Grt(A-2)–Spl(B-3)	9·0	840									M_2
	Grt(A-2)–Spl(B-4)	9·0	700									M_2
B223A(2)	Grt(C-18)–Opx(A-25)–Pl(C-54)	6·5		637	702	700	6·4	5·7			6·8	M_3
	Grt(C-18)–Opx(A-14)–Pl(C-54)	6·5		648	676	700	6·4	5·8			6·5	M_3
	Grt(C-18)–Opx(A-15)–Pl(C-54)	6·5		668	686	700	6·2	5·8			6·6	M_3
	Grt(C-35)–Opx(C-69)–Pl(A-19)	8·0		709	651	675	7·6	7·9			7·8	M_4
	Grt(C-35)–Opx(C-68)–Pl(A-19)	8·0		686	667	675	7·8	7·9			8·3	M_4
	Grt(C-70)–Opx(A-26)–Pl(A-19)	8·0		640	722	675	7·9	7·5			9·0	M_4
B12	Grt(B-8)–Opx(B-16)–Cpx(B-7)–Pl(B-5)	8·0		616	584	675	8·3	7·7	7·8	7·9	7·1	M_4
	Grt(A-5)–Opx(B-16)–Cpx(B-7)–Pl(B-5)	8·0		641	595	675	8·1	7·7	8·0	7·9	7·3	M_4
	Grt(A-6)–Opx(B-16)–Cpx(B-7)–Pl(B-5)	8·0		640	601	675	8·3	7·9	9·0	8·2	7·5	M_4

Abbreviations used for T (°C) and P (kbar) estimates: P_{Ref}/T_{Ref}: reference P and T; T_{GS}: temperature calculated using Grt–Spl–Crn–Sil geothermobarometer of Shulters & Bohlen (1989); T_P and P_P: temperature and pressure estimate following Pattison *et al.* (2003); HP: THERMOCALC, v.3·1, using thermodynamic dataset of Holland & Powell (1998); P_{FS}: GAFS assemblage; P_{ES}: GAES assemblage; P_{DI}: GADS assemblage; P_{HD}: GAHS assemblage; M: metamorphic stage.

the reactions (R2)–(R4) in the studied rocks depicts a counterclockwise P–T trajectory comprising heating (M_1), loading and cooling (M_2) (Fig. 11b).

M_2 metamorphic conditions can be further constrained from the coronal garnet$_2$ (core)–corundum–spinel$_1$–sillimanite$_1$ and garnet$_2$ (rim)–corundum–spinel$_2$–sillimanite$_2$ assemblages using the calibration of Shulters & Bohlen (1989), which gives a temperature range from ~910 to 700°C at 9 kbar pressure, respectively (Table 6). This range of temperature corresponds to the M_2 cooling event.

M_3 metamorphic conditions are estimated from orthopyroxene$_2$–plagioclase$_2$ symplectite and adjoining garnet composition in the presence of quartz. The results range from ~6·6 kbar, 700°C (Pattison *et al.*, 2003) to ~6·1 kbar, ~650°C (Holland & Powell, 1998). The authors have, therefore, taken an average P–T condition of ~6·4 kbar, ~675°C for this stage of metamorphism (Fig. 12c). This implies that the orthopyroxene$_2$–plagioclase$_2$ symplectite in the felsic granulite was possibly formed in response to decompression, and not by heating.

Application of the same methods for the composition of garnet$_2$ in the felsic granulite, and for coronal garnet in the mafic dyke$_1$, fails to distinguish between the T conditions of M_4 and those of M_3 (Table 6). This is clearly related to the problem of Fe–Mg diffusion's blocking temperature in coexisting garnet and orthopyroxene. However, the pressure estimate is approximately 1·5 kbar higher than that of M_3 (Fig. 12d and e; Table 6). Given the higher grossular content of garnet$_2$ and the depletion in An-content of plagioclase at the immediate contact, the authors interpret this difference in the pressure estimate as real (implying loading), and not an artefact of barometric computation.

ELECTRON MICROPROBE DATING OF MONAZITE

Samples and analytical procedure

Following the procedure outlined by Suzuki & Adachi (1991) and Montel *et al.* (1996), the authors have dated the metamorphic stages by electron probe analysis of monazite. Coarse monazite grains (100–140 μm grain diameter), occurring in four textural settings in the felsic granulite, were selected for this purpose. These are as follows. (1) Type 1 monazite, which occurs as inclusions within porphyroblastic garnet$_1$, and is expected to be protected from significant post-peak re-equilibration (Fig. 13a, Grain A; Table 8). (2) Type 2 monazite, which occurs in orthopyroxene$_2$–plagioclase$_2$ symplectite domains (Figs 4 and 13b; Table 8); Grain B of this textural type occurs in contact with a compositionally zoned

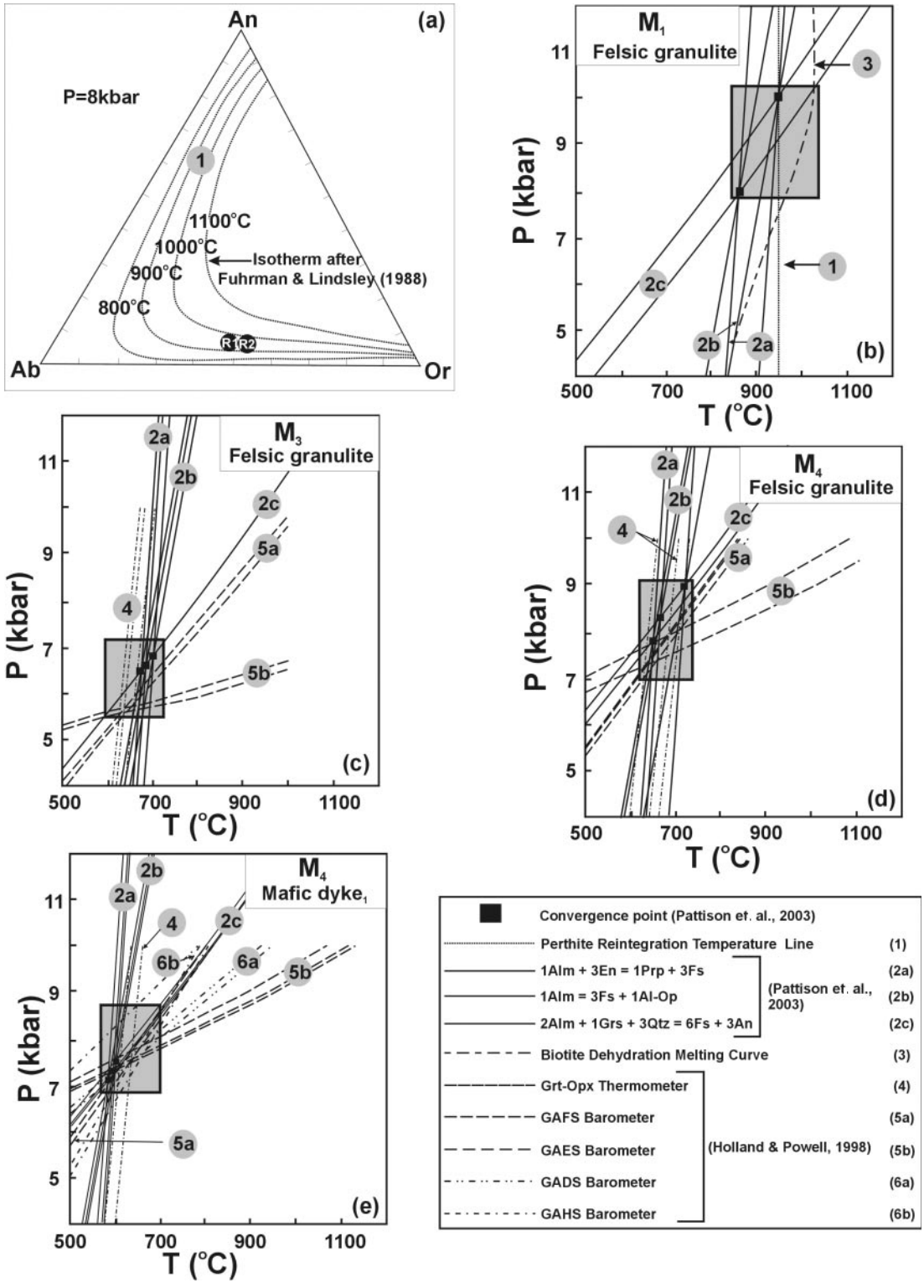

Fig. 12. The *P–T* conditions for M_1 (a and b), M_3 (c) and M_4 (d and e) metamorphism. In (a) R_1 and R_2 represent reintegrated compositions of mesoperthite, included within Grt_1 and in the matrix of the aluminous granulite, respectively. The mineral reactions and the methodologies, used for geothermobarometry, are shown in a box in the bottom right. Abbreviations used: GAFS, Garnet–Anorthite–Ferrosilite–Silica; GAES, Garnet–Anorthite–Enstatite–Silica; GADS, Garnet–Anorthite–Diopside–Silica; GAHS, Garnet–Anorthite–Hedenbergite–Silica.

Table 7: Balanced univariant reactions in the KFMASH system

System: KFMASH

Phases: Grt, Spl, Sil, Spr, Kfs, Crn, Bt, L

Excess phases: Sil, Kfs, L

Invariant point: (Crd, Opx)

Composition of phases:

- Grt: $Mg_{1·28}Fe_{1·72}Al_2Si_3O_{12}$
- Spl: $Mg_{0·25}Fe_{0·75}Al_2O_4$
- Sil: Al_2SiO_5
- Spr: $Mg_{1·34}Fe_{0·48}Al_{4·35}Si_{0·83}O_{10}$
- Kfs: $KAlSi_3O_8$
- Crn: Al_2O_3
- Bt: $K_{1·61}Mg_{3·83}Fe_{0·92}Al_{2·8}Si_{5·5}O_{18·76}(OH)_4$
- L: Melt composition after Carrington & Harley (1995)

Univariant reactions		ΔS ($JK^{-1}mol^{-1}$)	ΔV ($Jbar^{-1}$)	kbar/100°C
(Crd, Opx, Crn)	0·095Bt + 0·054Grt + 0·567Sil + 0·037Kfs = 0·124Spr + 0·068Spl + 0·37L (Crn)	266·48	2·12	12·55
(Crd, Opx, Spr)	0·095Bt + 0·328Spl + 1·085Sil + 0·037Kfs = 0·153Grt + 0·976Crn + 0·37L (Spr)	258·79	1·58	16·37
(Crd, Opx, Spl)	0·095Bt + 0·019Grt + 0·656Sil + 0·037Kfs = 0·168Crn + 0·103Spr + 0·37L (Spl)	264·94	2·03	13·07
(Crd, Opx, Bt)	0·3995Grt + 1·884Crn = 0·2393Spr + 0·7631Spl + Sil	14·46	1·04	1·39
(Crd, Opx, Grt)	0·095Bt + 0·035Spl + 0·702Sil + 0·037Kfs = 0·092Spr + 0·255Crn + 0·37L (Grt)	264·97	1·99	13·33

garnet (Fig. 9d); Grain B_1 occurs as narrow, curvilinear grains in the same symplectite domain. (3) Type 3 monazite occurs as large grains in the strain shadow domains, away from the influence of BS_3 mylonite fabric (Fig. 4). (4) Type 4 monazite occurs in the BS_3 mylonite fabric (Fig. 4).

All analyses were carried out with a Camebax Microbeam Electron Microprobe at the University of Bonn, Germany. The instrumental operating conditions and the analytical procedures were outlined by Dobmeier & Simmat (2002). The data are presented both as spot chemical ages in individual monazite grains and also by the *Ch*emical Th–U–total Pb *I*sochron *Me*thod (CHIME method after Suzuki *et al.*, 1994; Cocherie *et al.*, 1998).

RESULTS

A total of 183 measurements on 11 grains were carried out (Table 8). Grain A, belonging to Type 1 monazite, shows euhedral crystal outline with concentric zonation (Fig. 13a). Th, U, Pb profiling along direction A–B indicates that the colour variation is primarily due to Th-zoning, with the brightest regions related to the highest Th concentrations (Fig. 14a). The analysed spots show variations in Th content from 5·66 to 11·01 wt %. In all the spots, the Pb content (0·64–1·29 wt %) is significantly above the detection limit. Spot chemical ages show a concordant age population in the range 1970–2177 Ma (Fig. 15a). Using this dataset, the calculated CHIME ages give a rather tightly constrained age of 2089 ± 14 Ma for the formation of Grain A (Fig. 16a).

The back-scattered electron image of grain B, belonging to Type 2 monazites, shows three distinct compositional domains from core to rim (Fig. 13b). (1) An ovoid relatively homogeneous core (Domain 1, Fig. 13b) is present, showing broadly uniform Th and Pb concentrations of 7·10–9·05 and 0·79–0·96 wt %, respectively (Fig. 14b). Spot chemical ages from this domain range from 1958 to 2208 Ma (Fig. 15b). Using the CHIME method, the 17 analysed spots give a tightly constrained age of 2086 ± 16 Ma (Fig. 16b). (2) An inner concentric, Th-zoned rim with locally preserved euhedral outline is present in Grain B (Domain 2, Figs 13b and 14b–d). This domain resembles Type 1 monazites described above. Profile E–F shows that the domain is thinly banded close to its contact with the previous domain, and there is a thick outer rim, best developed in its lower part (Fig. 14d). Spot chemical ages from this domain range from 1924 to 2299 Ma (Fig. 15b), which give a CHIME chemical age of ∼2040 ± 17 Ma (Fig. 16c). This age is nearly 40 Myr younger relative to the previous domain. Consequently, Domain 1 of Grain B is considered to be an inherited older core. (3) An outermost homogeneous dark rim (Domain 3, Fig. 13b) of substantially lower Pb (0·20–0·48 wt %) and also Th (4·12–5·89 wt %)

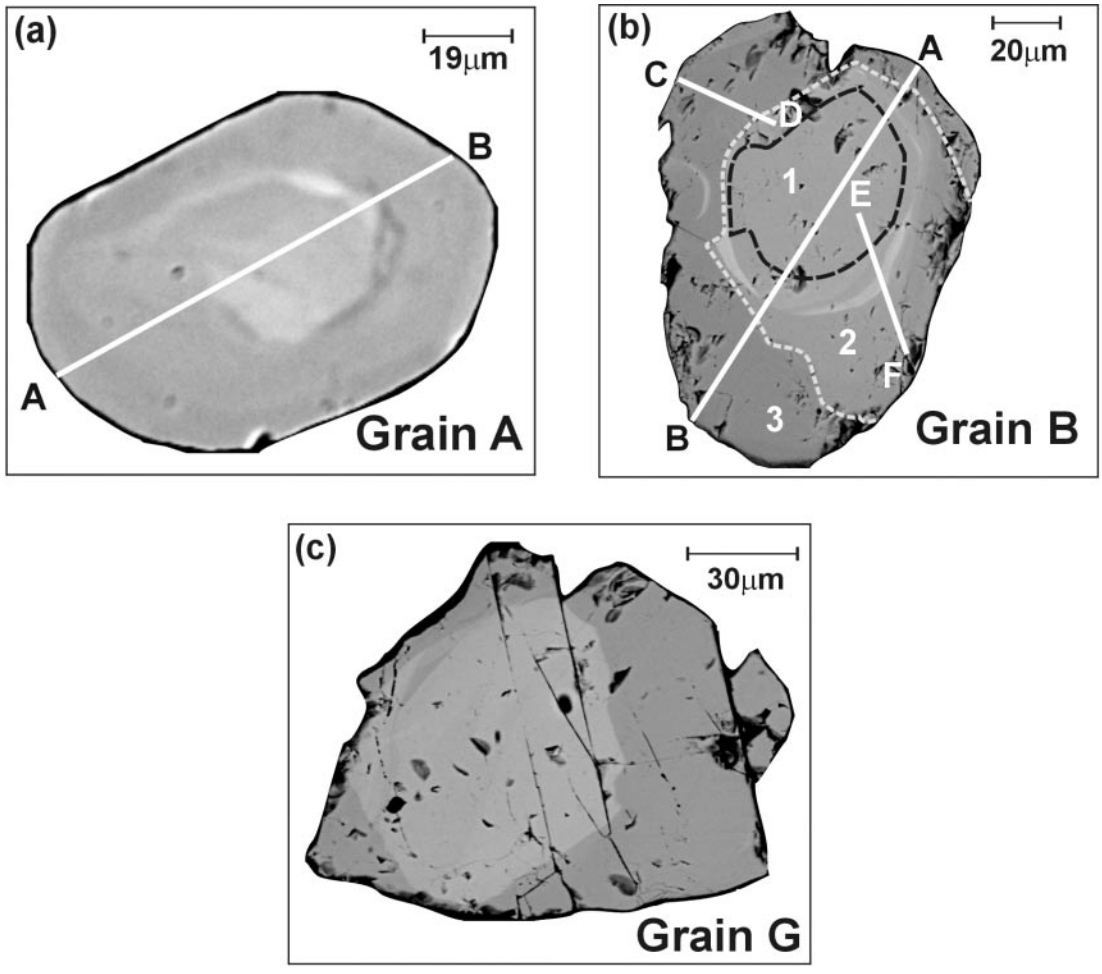

Fig. 13. Back-scattered electron images (BSE) of monazites occurring in different textural locations in the felsic granulites. A–B [in (a)] and A–B, C–D and E–F [in (b)] are the locations of Th–U–Pb compositional and age profiles, shown in Fig 14. 1, 2 and 3 in (b) refer to three distinct compositional and age domains in monazite Grain B (see text for details).

concentrations is present (Fig. 14b and c). The boundary between this domain and Domain 2 is sharp—typically a few microns thick, as shown in the two compositional profiles A–B and C–D (Fig. 14b and c)—and has truncated the concentric zoning of Domain 2 (Fig. 13b). Considering the sharpness of the boundary between the domains and the occurrence of Domain 3 in direct contact with garnet$_2$, the authors interpret the formation of Domain 3 as a consequence of re-metamorphism (M_4), and not due to Pb-diffusion (Braun *et al.*, 1998; Cocherie *et al.*, 1998; Crowley & Ghent, 1999). This domain gives distinct Mesoproterozoic spot chemical ages in the range 1318–1648 Ma (Fig. 15b). Calculated CHIME monazite ages give a tightly constrained age of 1525 ± 13 Ma (Fig. 16d).

Type 3 monazite (Grain G, Fig. 13c; Table 8) also shows a homogeneous core that gives a CHIME age of 2048 ± 14 Ma (Figs 15c and 16e); this has a Mesoproterozoic metamorphic overgrowth (Fig. 15c). Type 4 monazites, excepting Grain D, show consistent Mesoproterozoic age (Table 8). Grain D shows a relict Palaeoproterozoic core and rim of Mesoproterozoic age (Table 8). An isochron drawn through these monazite compositions gives an age of 1450 ± 9 Ma (Fig. 16f).

Summarizing, the monazite grains of variable compositional characteristics in different textural settings in the studied rocks bear the imprint of a Mesoproterozoic (1450–1525 Ma) metamorphism superimposed on a Palaeoproterozoic (2040–2090 Ma) event. Based on (a) the occurrence of Type 1 monazites as shielded inclusions within garnet$_1$ and (b) the presence of concentric Th-zonation in the former and also in Domain 2 of Type 2 monazites, the authors interpret a Palaeoproterozoic age for the UHT metamorphism, M_1. In contrast, the Mesoproterozoic ages, which are retrieved from metamorphic overgrowths, and the BS_3 mylonite domain mark the M_4 metamorphism. These results will be combined with textural, compositional and

Table 8: Electron microprobe data for analysed monazites in felsic granulites

Sample no.	Spot no.	Th (wt %)	Pb (wt %)	U (wt %)	Y (wt %)	Age (Ma)	PbO_{COR}	ThO_2^*	Metamorphic history	Textural site
B42B(1)										
A	7	6·51	0·74	0·32	0·10	2051	0·79	8·80	Leucosome	Inclusion in Grt_1
	8	11·01	1·29	0·45	1·21	2146	1·38	14·50	crystallization (M_1)	
	9	8·10	0·94	0·33	1·63	2114	0·99	10·67		
	10	7·88	0·89	0·36	1·32	2036	0·95	10·53		
	11	8·06	0·95	0·33	0·94	2157	1·01	10·64		
	12	6·12	0·74	0·35	0·08	2120	0·80	8·51		
	13	8·12	0·91	0·32	0·95	2068	0·97	10·62		
	14	7·62	0·91	0·36	1·63	2127	0·96	10·26		
	15	7·13	0·86	0·51	0·12	2033	0·92	10·34		
	17	5·99	0·72	0·28	0·05	2175	0·78	8·05		
	18	6·19	0·74	0·31	0·06	2143	0·79	8·40		
	19	6·59	0·77	0·36	0·08	2070	0·83	9·07		
	20	6·56	0·75	0·35	0·07	2037	0·81	8·99		
	21	5·66	0·65	0·28	0·05	2069	0·70	7·67		
	22	6·53	0·76	0·35	0·06	2070	0·81	8·93		
	23	6·66	0·80	0·37	0·05	2118	0·86	9·21		
	24	7·34	0·85	0·51	0·13	1970	0·91	10·54		
	25	6·29	0·76	0·29	0·08	2189	0·82	8·43		
	26	8·55	0·99	0·33	1·60	2125	1·05	11·18		
	27	6·77	0·82	0·38	0·07	2131	0·89	9·38		
	28	6·22	0·70	0·34	0·03	2002	0·75	8·56		
	29	8·23	0·94	0·34	1·35	2085	1·00	10·85		
	30	5·71	0·64	0·25	0·10	2057	0·69	7·59		
	31	9·25	1·09	0·34	1·50	2177	1·16	12·02		
	32	7·11	0·82	0·44	0·09	2004	0·88	10·00		
B223A(2)										
B	11	7·56	0·87	0·23	0·01	2203	0·94	9·62	Older inherited core	Relict within M_3
	12	8·10	0·87	0·23	—	2075	0·94	10·23		symplectite (Domain 1)
	13	8·08	0·88	0·28	—	2067	0·95	10·42		
	14	8·21	0·84	0·23	—	2082	0·96	10·39		
	15	7·91	0·87	0·26	0·01	1958	0·94	10·13		
	16	7·99	0·87	0·26	—	2070	0·94	10·23		
	17	7·94	0·89	0·24	0·00	2138	0·96	10·11		
	19	7·65	0·88	0·22	0·00	2208	0·95	9·70		
	32	7·97	0·85	0·24	—	2058	0·92	10·12		
	46	8·10	0·85	0·23	—	2035	0·92	10·23		
	47	8·20	0·91	0·26	—	2128	0·98	10·46		
	49	8·01	0·88	0·26	—	2088	0·94	10·22		
	50	9·05	0·96	0·28	—	2035	1·03	11·50		
	51	8·21	0·84	0·23	—	1997	0·91	10·32		
	67	7·92	0·80	0·20	0·05	1971	0·86	9·87		
	68	7·10	0·79	0·21	0·02	2127	0·85	9·01		
	69	8·30	0·90	0·26	0·05	2064	0·96	10·58		

Table 8: continued

Sample no.	Spot no.	Th (wt %)	Pb (wt %)	U (wt %)	Y (wt %)	Age (Ma)	PbO_{COR}	ThO_2^*	Metamorphic history	Textural site
B	7	6·78	0·75	0·24	—	2080	0·81	8·77	Leucosome	(Domain 2)
	8	6·81	0·73	0·22	—	2055	0·79	8·69	crystallization (M_1)	
	9	9·08	0·96	0·23	0·00	2061	1·03	11·33		
	10	8·63	0·89	0·26	—	1996	0·96	10·95		
	20	7·86	0·95	0·25	—	2299	1·03	10·05		
	22	8·19	0·82	0·26	—	1924	0·89	10·45		
	23	7·67	0·79	0·21	—	2007	0·85	9·65		
	33	8·01	0·82	0·26	—	1965	0·89	10·22		
	42	6·75	0·70	0·26	—	1952	0·75	8·78		
	43	6·93	0·74	0·23	—	2039	0·80	8·88		
	44	9·74	1·01	0·26	—	2020	1·09	12·21		
	45	9·32	1·01	0·27	—	2084	1·08	11·77		
	48	6·74	0·71	0·23	—	1990	0·76	8·67		
	52	10·88	1·08	0·30	—	1942	1·17	13·66		
	53	11·86	1·18	0·23	—	1983	1·27	14·48		
	54	7·09	0·79	0·24	—	2118	0·85	9·10		
	55	6·85	0·72	0·24	—	2004	0·78	8·81		
	56	6·21	0·68	0·25	—	2033	0·73	8·15		
	58	7·43	0·80	0·23	—	2059	0·86	9·45		
	59	6·99	0·71	0·23	—	1954	0·77	8·92		
	60	5·15	0·58	0·34	—	1946	0·63	7·30		
	62	6·57	0·76	0·22	0·02	2189	0·82	8·44		
	63	8·90	0·94	0·26	0·03	2036	1·01	11·25		
	64	8·13	0·94	0·22	0·03	2219	1·01	10·24		
	65	7·98	0·91	0·19	0·05	2230	0·98	9·94		
	66	7·93	0·90	0·24	0·03	2168	0·97	10·10		
	70	8·27	0·89	0·22	0·00	2080	0·95	10·39		
	71	9·04	0·95	0·20	0·00	2073	1·02	11·16		
	72	8·98	0·94	0·27	0·01	2013	1·01	11·37		
	73	8·67	0·94	0·24	0·01	2096	1·01	10·91		
	74	8·20	0·95	0·26	0·03	2195	1·02	10·48		
	75	6·75	0·71	0·24	0·04	1992	0·77	8·72		
	76	6·45	0·70	0·24	0·04	2031	0·75	8·38		
	80	13·57	1·32	0·31	0·03	1932	1·43	16·75		
	81	8·74	0·89	0·26	0·02	1974	0·96	11·07		
B	1	4·35	0·35	0·15	0·08	1554	0·38	5·57	Metamorphic	(Domain 3)
	2	4·44	0·35	0·16	—	1515	0·38	5·72	overgrowth (M_4)	
	3	4·34	0·36	0·13	0·09	1615	0·39	5·48		
	4	4·43	0·36	0·23	—	1500	0·39	5·99		
	5	4·40	0·39	0·37	0·10	1496	0·42	6·51		
	6	4·47	0·41	0·41	—	1493	0·44	6·74		
	21	5·73	0·42	0·14	0·03	1461	0·45	7·11		
	24	5·88	0·45	0·22	—	1475	0·49	7·59		
	25	5·72	0·47	0·25	—	1540	0·51	7·54		
	26	5·81	0·48	0·21	—	1594	0·52	7·48		
	27	5·60	0·45	0·22	—	1522	0·48	7·26		

Sample no.	Spot no.	Th (wt %)	Pb (wt %)	U (wt %)	Y (wt %)	Age (Ma)	PbO_{COR}	ThO_2^*	Metamorphic history	Textural site
	28	4·61	0·35	0·20	—	1436	0·38	6·04		
	29	4·45	0·35	0·12	—	1545	0·37	5·55		
	30	4·70	0·34	0·09	—	1480	0·37	5·73		
	31	4·67	0·34	0·09	—	1481	0·37	5·67		
	34	5·89	0·46	0·16	—	1553	0·50	7·36		
	35	4·74	0·35	0·11	—	1487	0·38	5·83		
	36	4·64	0·37	0·13	—	1555	0·393	5·80		
	37	4·64	0·36	0·08	—	1577	0·36	5·62		
	38	4·24	0·41	0·31	—	1648	0·44	6·11		
	39	4·34	0·37	0·38	—	1416	0·40	6·46		
	40	4·34	0·42	0·39	—	1648	0·45	6·56		
	41	4·34	0·40	0·38	—	1519	0·43	6·50		
	57	5·15	0·47	0·33	—	1604	0·51	7·24		
	61	2·73	0·20	0·15	0·08	1318	0·21	3·70		
	77	4·15	0·38	0·43	0·11	1458	0·41	6·46		
	78	4·21	0·41	0·43	0·12	1560	0·45	6·56		
	79	4·12	0·44	0·44	0·08	1654	0·47	6·50		
B_1	1	2·99	0·24	0·13	0·08	1490	0·26	3·94	M_4	M_3 symplectite
	2	5·81	0·47	0·27	0·16	1518	0·51	7·71		
	3	3·50	0·29	0·16	0·04	1544	0·31	4·64		
	4	3·20	0·25	0·14	0·04	1446	0·27	4·22		
	5	3·11	0·22	0·10	0·07	1360	0·23	3·94		
	13	3·18	0·24	0·12	0·05	1461	0·26	4·12		
	14	3·27	0·26	0·14	0·05	1494	0·28	4·29		
	15	2·13	0·16	0·09	0·07	1428	0·17	2·77		
	16	6·53	0·50	0·29	0·22	1447	0·54	8·59		
	17	2·62	0·20	0·13	0·11	1449	0·22	3·49		
G	4	10·02	1·04	0·26	0·02	2027	1·12	12·53	Inherited core	Matrix monazite
	5	10·64	1·14	0·25	0·04	2104	1·23	13·20		
	6	10·58	1·11	0·27	0·02	2050	1·20	13·21		
	7	10·46	1·10	0·27	0·01	2053	1·19	13·08		
	8	11·34	1·17	0·29	0·03	2018	1·26	14·16		
	9	11·31	1·16	0·31	0·03	1995	1·25	14·21		
	11	11·45	1·22	0·32	0·04	2063	1·31	14·42		
	12	11·99	1·28	0·30	0·04	2086	1·38	14·95		
G	3	5·58	0·44	0·17	0·03	1542	0·47	7·05	Metamorphic	
	13	6·14	0·47	0·15	0·15	1527	0·51	7·60	overgrowth (M_4)	
	14	6·19	0·46	0·12	0·03	1509	0·50	7·54		
	15	5·13	0·38	0·25	0·02	1377	0·41	6·85		
	16	6·31	0·43	0·13	0·04	1383	0·46	7·71		
	17	6·98	0·49	0·12	0·05	1439	0·53	8·43		
D	26	5·69	0·75	0·56	0·14	2061	0·81	8·91	Leucosome	Large grain in
	28	10·56	1·06	0·28	0·00	1949	1·14	13·24	crystallization	mylonite fabric, BS_3
	29	4·02	0·45	0·25	0·06	1959	0·49	5·64		

Table 8: continued

Sample no.	Spot no.	Th (wt %)	Pb (wt %)	U (wt %)	Y (wt %)	Age (Ma)	PbO_{COR}	ThO_2*	Metamorphic history	Textural site
	30	8·09	0·84	0·25	0·02	1998	0·91	10·29		
	34	4·04	0·63	0·71	0·26	1998	0·67	7·68		
	35	6·92	0·71	0·28	0·21	1924	0·77	9·06		
D	27	6·20	0·45	0·17	0·14	1437	0·48	7·75	Metamorphic	
	31	5·54	0·41	0·19	0·15	1442	0·44	7·07	overgrowth (M_4)	
	32	6·31	0·46	0·12	0·04	1479	0·49	7·67		
	33	6·28	0·46	0·10	0·05	1501	0·49	7·54		
E	12	6·04	0·44	0·17	0·18	1449	0·48	7·57	M_4	Mylonite fabric, BS_3
	13	8·80	0·61	0·18	0·08	1407	0·66	10·74		
	14	7·29	0·50	0·11	0·00	1412	0·54	8·74		
	15	7·51	0·54	0·14	0·01	1460	0·58	9·12		
	16	10·57	0·78	0·16	0·00	1527	0·84	12·69		
	17	10·84	0·78	0·15	0·02	1488	0·84	12·96		
	18	10·99	0·78	0·15	0·01	1465	0·84	13·10		
	19	7·18	0·51	0·13	0·01	1451	0·55	8·68		
	20	7·93	0·57	0·11	0·01	1484	0·61	9·48		
	21	6·34	0·45	0·19	0·17	1378	0·48	7·98		
	22	5·72	0·45	0·19	0·14	1508	0·48	7·30		
	23	7·85	0·56	0·12	0·02	1465	0·60	9·40		
	24	10·60	0·77	0·17	0·02	1490	0·83	12·74		
H	3	6·51	0·48	0·15	0·14	1478	0·52	8·02	M_4	Mylonite fabric, BS_3
	4	5·96	0·45	0·19	0·05	1473	0·48	7·56		
	5	5·55	0·39	0·13	0·06	1411	0·42	6·84		
	6	5·28	0·37	0·09	0·09	1435	0·40	6·37		
	7	5·23	0·38	0·09	0·04	1487	0·41	6·32		
	8	5·14	0·36	0·10	0·05	1425	0·39	6·26		
	9	10·40	0·75	0·14	0·03	1495	0·81	12·41		
	10	5·70	0·40	0·18	0·12	1373	0·43	7·21		
	11	5·20	0·35	0·10	0·03	1373	0·38	6·32		
	12	5·62	0·35	0·16	0·05	1238	0·38	7·03		
	13	5·16	0·34	0·11	0·05	1327	0·36	6·32		
	14	5·14	0·36	0·10	0·05	1408	0·38	6·26		
	15	4·98	0·34	0·11	0·05	1360	0·36	6·12		
	16	5·08	0·36	0·12	0·05	1422	0·39	6·26		
	17	5·05	0·35	0·12	0·06	1392	0·38	6·22		
	18	6·11	0·42	0·17	0·09	1365	0·45	7·62		
I	1	6·55	0·47	0·11	0·01	1472	0·51	7·90	M_4	Mylonite fabric, BS_3
	2	6·32	0·47	0·11	0·01	1521	0·51	7·64		
	36	5·61	0·40	0·12	0·06	1448	0·43	6·86		
	37	6·78	0·47	0·19	0·18	1375	0·51	8·50		
	38	6·31	0·45	0·11	0·00	1475	0·49	7·62		
J	20	4·34	0·31	0·18	0·14	1360	0·33	5·66	M_4	Mylonite fabric, BS_3
	21	3·56	0·28	0·18	0·14	1443	0·30	4·80		

PbO_{COR}: Pb-correction after Dobmeier & Simmat (2002). *ThO_2 after Suzuki *et al*. (1994); Cocherie *et al*. (1998).

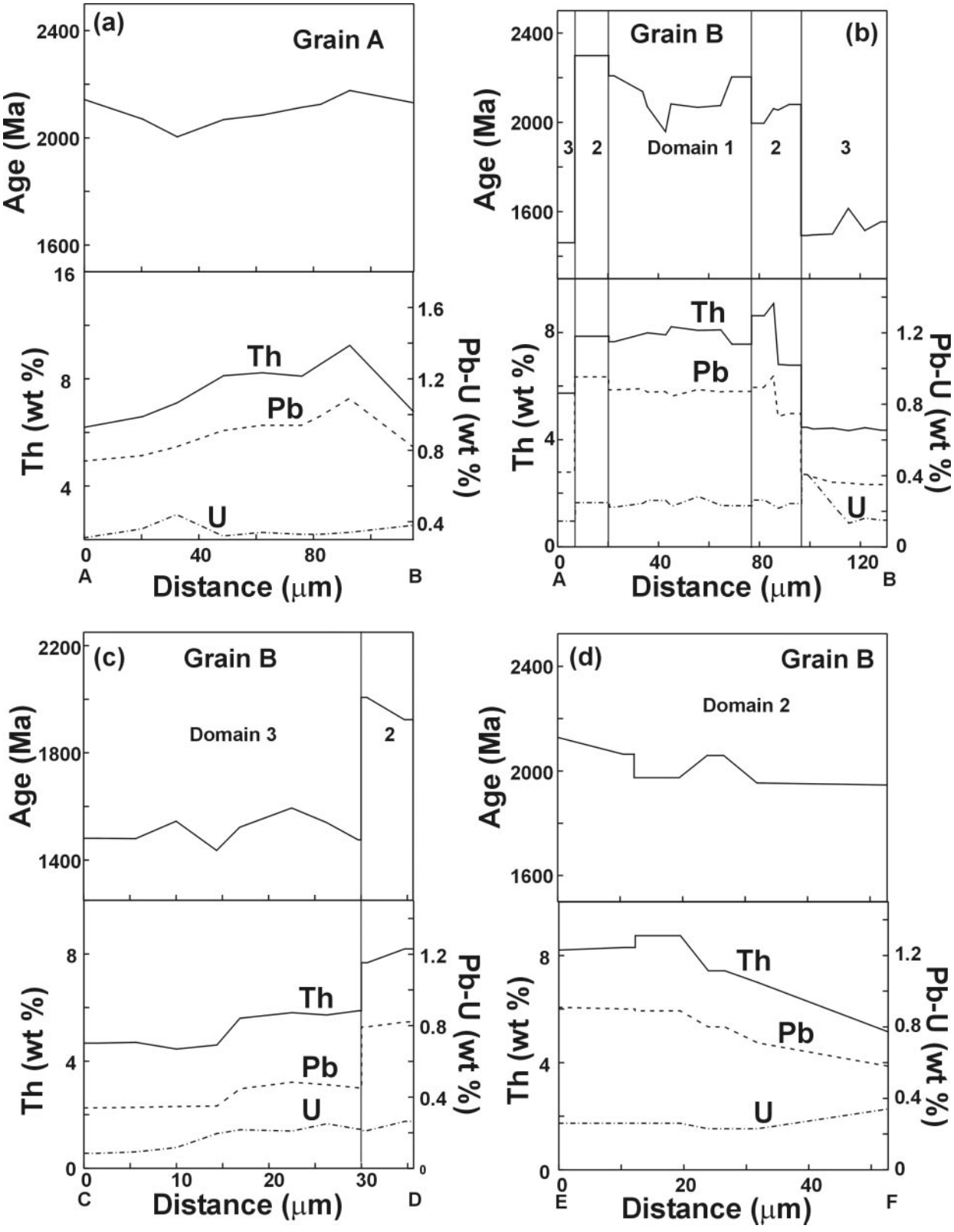

Fig. 14. Th, U, Pb compositional and age profiles for Grain A (a) and Grain B (b–d).

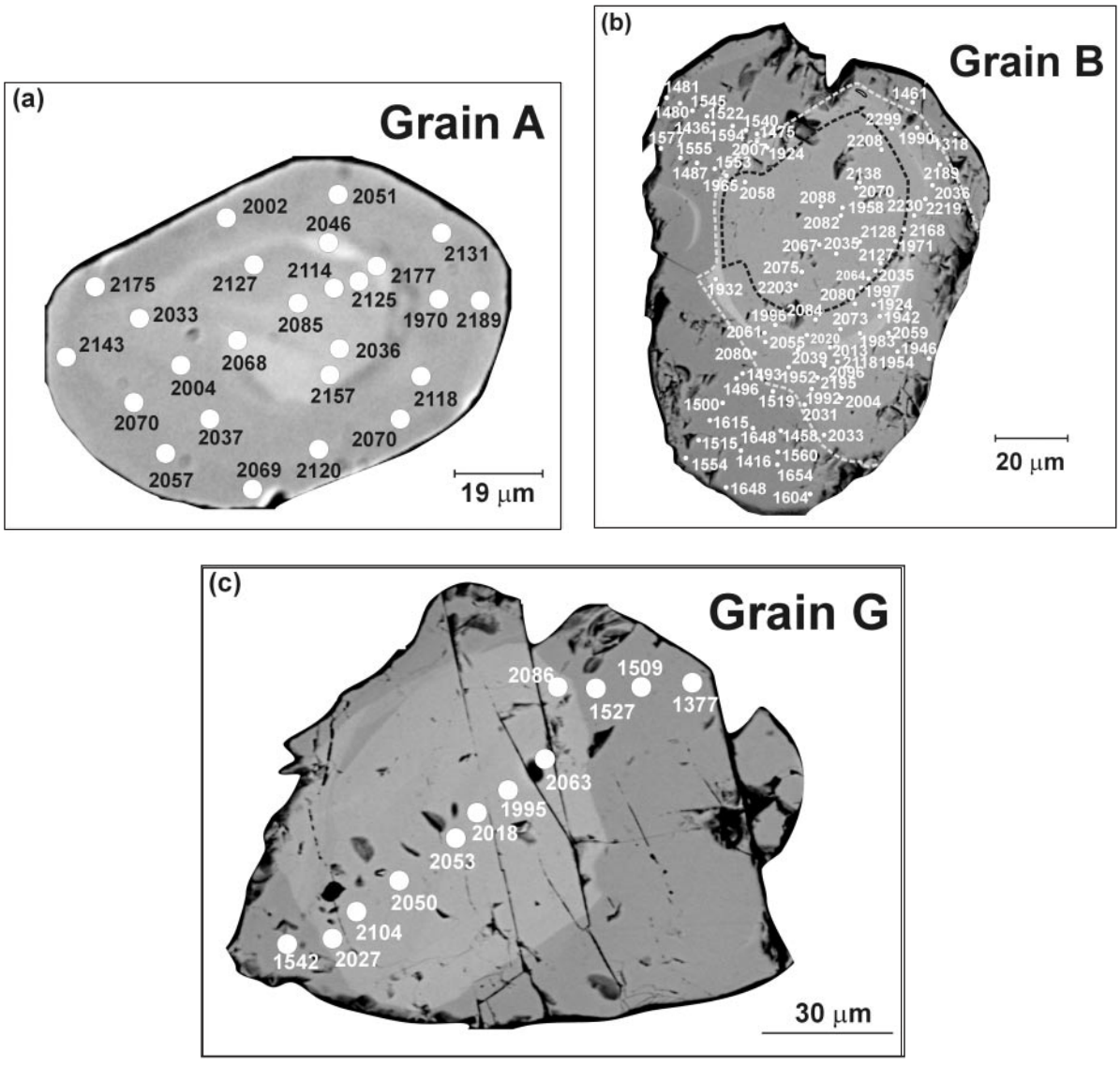

Fig. 15. Spot chemical ages for Grains A, B and G (see Table 8 and text for details).

thermobarometric data to constrain the integrated metamorphic history of the studied complex, and its implication.

DISCUSSION

This study demonstrates that the allochthonous BBG domain at the southern periphery of the CITZ records two distinct granulite-facies tectonothermal events, separated by a time gap of approximately 500 Myr. Geothermobarometric data and interpretation of reaction textures in the context of appropriate petrogenetic grids constrain the earlier UHT granulite-facies metamorphism (M_1) at $P \sim 9$ kbar, $T \sim 950°C$, followed by a subsequent near-isobaric cooling event (M_2), which was terminated at ~700°C (Fig. 17a). Considering that near isobaric cooling from T_{Max} is a natural consequence of thermal relaxation of the perturbed geotherm, the M_1–M_2 metamorphic stages can be considered to belong to the same UHT metamorphic event. Based on the partial KFMASH petrogenetic grid, and the sequential operation of reactions (R2)–(R4), the authors infer an overall counterclockwise P–T path for rocks metamorphosed during the UHT event based on the deduced deep crustal heating–cooling trajectory (Fig. 17a) (Waters, 1989; Dasgupta *et al.*, 1997; Sengupta *et al.*, 1999). Electron microprobe dating of monazites constrains an age of 2040–2090 Ma for this UHT metamorphic event. Our results, therefore, provide the first tight constraint on the

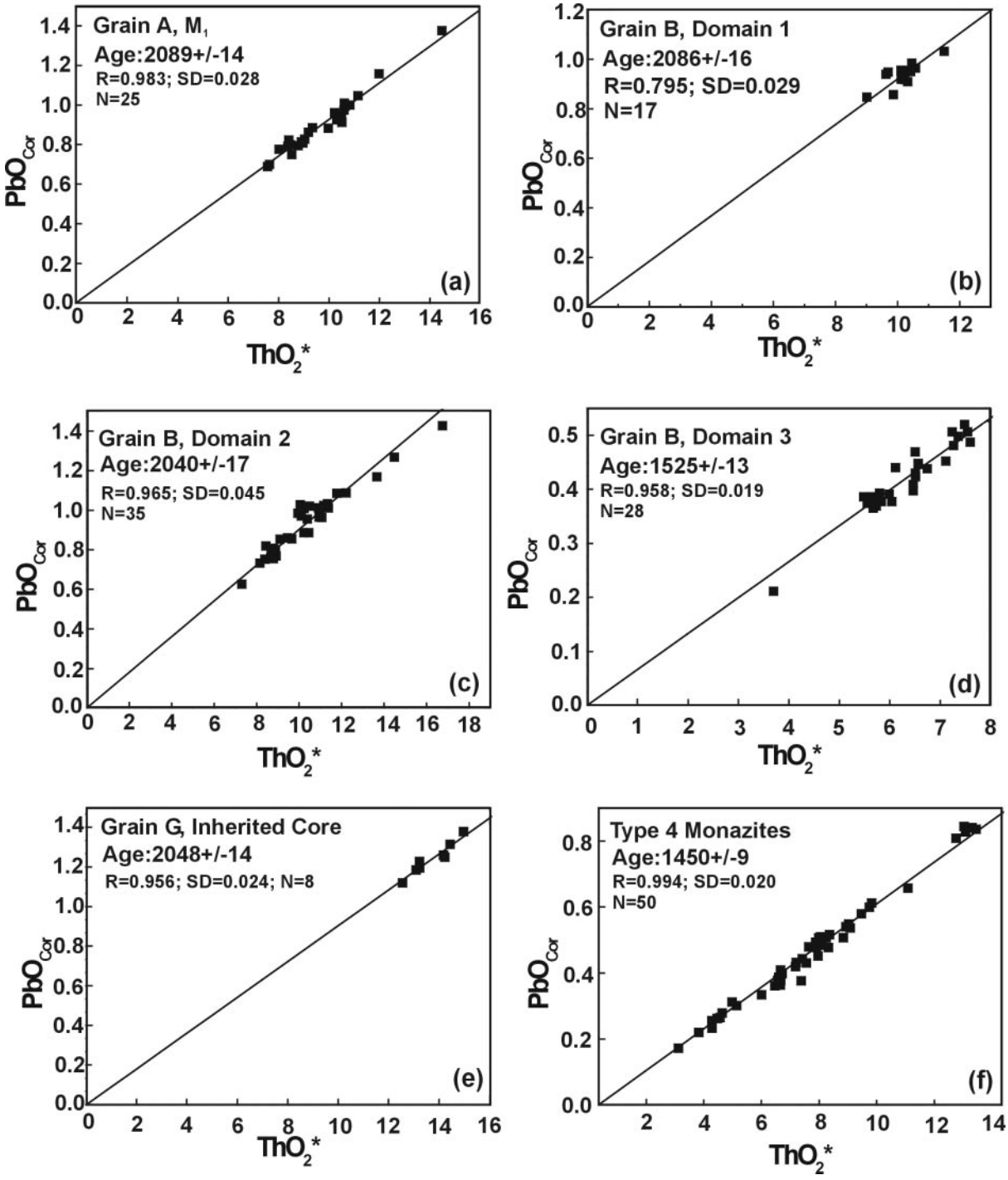

Fig. 16. The CHIME monazite ages for different metamorphic stages using the PbO_{COR} vs ThO_2^* plot (after Suzuki *et al.*, 1994; Cocherie *et al.*, 1998). PbO_{COR} refers to the corrected PbO by eliminating the likely overlap of YL_γ on PbM_α during WDS-scans and following the approach of Dobmeier & Simmat (2002). ThO_2^* is the sum of the measured ThO_2 and an equivalent ThO_2, after conversion of the measured UO_2 content of each analysed spot (see text for details).

presence of an older crust, and a Palaeoproterozoic crustal history in the rocks leading to cratonization (stabilization through isobaric cooling) of the CITZ. Similar Palaeoproterozoic UHT metamorphism on a counterclockwise *P–T* path has been documented from elsewhere (Australia: Goscombe, 1992; Labrador: Currie & Gittins, 1988), and this suggests a global thermal perturbation at this time (Condie, 2000; Windley, 2003).

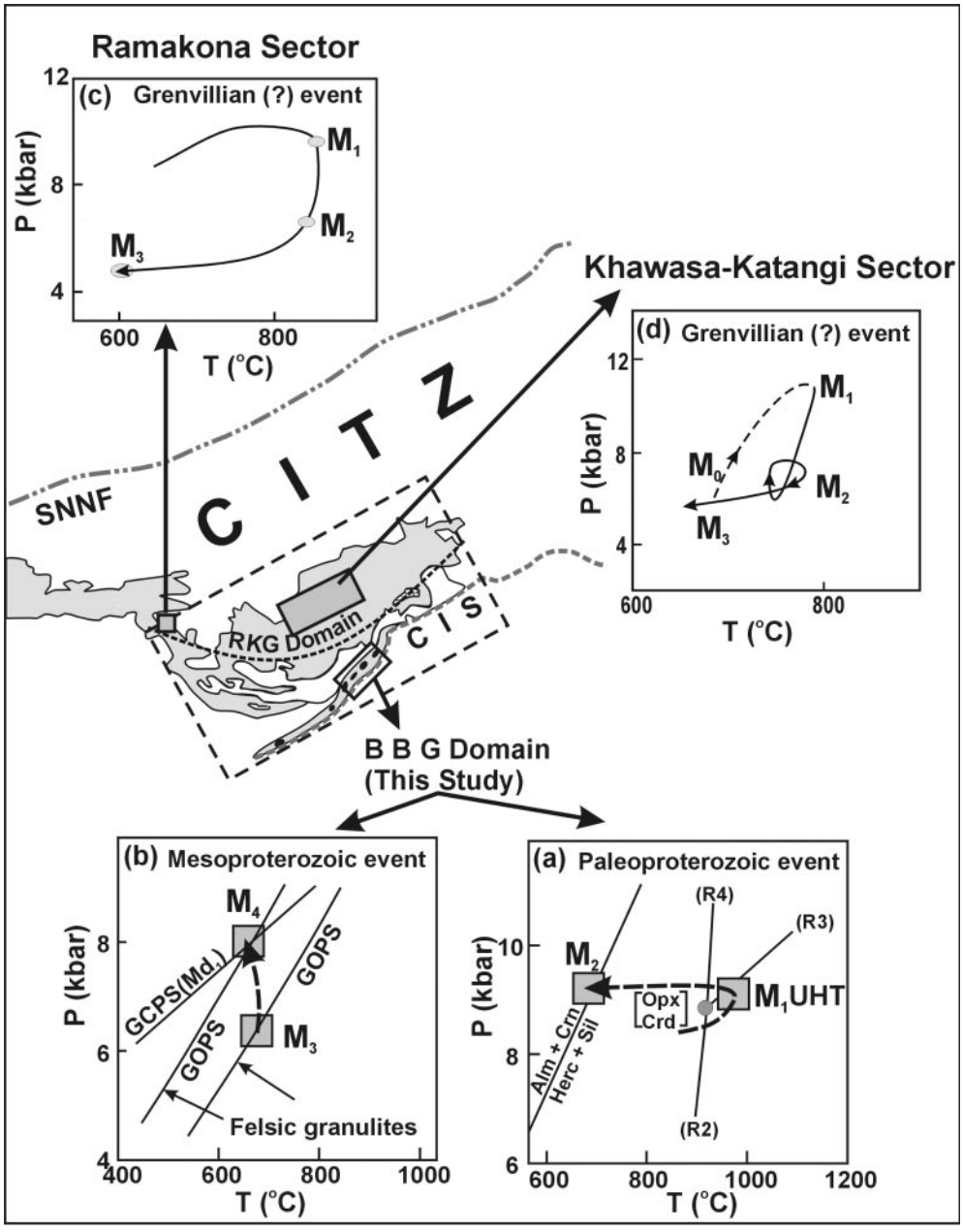

Fig. 17. Contrasting tectonothermal histories in the Sausar Mobile Belt. The southern Bhandara–Balaghat granulite (BBG) domain records a Palaeoproterozoic UHT metamorphic event, bearing imprints of a deep crustal heating–cooling *P–T* path (a) and its subsequent reworking in the Mesoproterozoic (b) (this study). In contrast, rocks from the northern Ramakona–Katangi granulite (RKG) domain preserve a clockwise *P–T* loop (c and d) of possibly Grenvillian age (Bhowmik & Roy, 2003; Bhowmik & Spiering, 2004). Abbreviations used: (R2), (R3) and (R4), reactions in aluminous granulites (see text); GOPS, reaction Opx + Pl = Grt + Qtz in felsic granulite; GCPS, reaction Cpx + Pl = Grt + Qtz in mafic dyke$_1$.

The isobarically cooled deep crustal UHT granulites were subsequently affected by decompression down to 6·4 kbar at 675°C during M_3 and loading to 8 kbar during M_4. Electron microprobe dating of monazite gives an age of 1450–1525 Ma for M_4. This implies that the isobarically cooled granulites were residing at lower-crustal depths (corresponding to 9 kbar metamorphic pressure) for approximately 500 Myr before being partially exhumed by the later Mesoproterozoic tectonothermal event. The mafic dykes were emplaced within this time interval and were affected by the later event, M_4. M_3 could not be dated directly. However,

M_3 with its decompressive retrograde *P–T* path appears to be unrelated to the Palaeoproterozoic cooling of M_2. The authors would, therefore, consider M_3 and M_4 to be part of the same Mesoproterozoic tectonothermal event (Fig. 17b). This interpretation supports the prediction of Harley (1989) that isobarically cooled lower-crustal granulites must await a separate orogeny for exhumation. The overall *P–T* path of the Mesoproterozoic metamorphism remains indeterminate because the prograde arm cannot be characterized. Nevertheless, the granulites were still at depths corresponding to 8 kbar pressure during Mesoproterozoic time, and their final exhumation required further tectonothermal events. There is an increasing body of evidence that similar Mesoproterozoic granulite-facies metamorphism is more common (East Antarctica: Kelly *et al.*, 2002; Eastern Ghats Belt, India: Mezger & Cosca, 1999; Kovach *et al.*, 2001; Simmat, 2003, quoted by Dobmeier & Raith, 2003) than originally believed.

The tectonothermal history of the granulite complex of the BBG domain, deduced in this study, contrasts sharply with that from the northern granulite (RKG) domain of the SMB (Fig. 17c and d) (Bhowmik & Roy, 2003; Bhowmik & Spiering, 2004). The latter is characterized by a clockwise *P–T* trajectory of possible Grenvillian age (Fig. 17c and d). These two granulite domains are separated by the greenschist–amphibolite-facies Sausar Group (Fig. 1) metamorphosed during the *ca.* 1000 Ma Grenvillian event (Lippolt & Hautman, 1994; Pandey *et al.*, 1998). It may be recalled that the BD_4–BD_5 deformations in the BBG granulites studied here are also recorded in the Sausar Group rocks. This raises the possibilities that (a) these two deformations are of Grenvillian age, (b) the two granulite domains and the Sausar Group rocks were juxtaposed during this collisional event along the CITZ, and (c) the BBG granulites were exhumed to shallower crustal levels at this time and (d) the Grenvillian orogeny appears to be responsible for the formation of the Indian subcontinent through collision of the SIB and NIB (Fig. 1) along the CITZ. On a larger scale, the Central Indian Tectonic Zone appears to record nearly 1000 Myr of multistage crustal evolutionary history in the Proterozoic.

ACKNOWLEDGEMENTS

We acknowledge the financial assistance from the DST (Grant No. ESS/23/VES/129/2000) and DAAD (S.K.B.), IIT, Kharagpur (A.B.S.), Mineralogisch–Petrologisches Institüt (B.S.) and DFG (M.M.R.). The work was completed when SKB was in the Mineralogisch–Petrologisches Institut, Bonn, as a visiting fellow under INSA–DFG fellowship. Part of the analytical work was also carried out in the Geological Survey of India, for which we thank N. C. Pant and S. Shome for extending help during microprobe analysis and backscattered electron image photography. X-ray element maps were generated in the University of Cologne, for which we thank Markus Klein. The manuscript has benefited greatly from stimulating discussions with Somnath Dasgupta. We would also like to thank two anonymous reviewers for thorough and constructive reviews, and Richard Arculus for editorial assistance.

REFERENCES

Bhowmik, S. K. & Pal, T. (2000). Petrotectonic implication of the granulite suite north of the Sausar mobile belt in the overall tectonothermal evolution of the Central Indian mobile belt. *Geological Survey of India Unpublished Progress Report.*

Bhowmik, S. K. & Roy, A. (2003). Garnetiferous metabasites from the Sausar Mobile Belt: petrology, *P–T* path and implications for the tectonothermal evolution of the Central Indian Tectonic Zone. *Journal of Petrology* **44**, 387–420.

Bhowmik, S. K. & Spiering, B. (2004). Constraining the prograde and retrograde *P–T* paths of granulites using decomposition of initially zoned garnets: an example from the Central Indian Tectonic Zone. *Contributions to Mineralogy and Petrology* **147**, 581–603.

Braun, I., Montel, J. M. & Nicollet, C. (1998). Electron microprobe dating of monazites from high-grade gneisses and pegmatites of the Kerala Khondalite Belt, southern India. *Chemical Geology* **146**, 65–85.

Carrington, D. P. & Harley, S. L. (1995). Partial melting and phase relations in high-grade metapelites: an experimental petrogenetic grid in the KFMASH system. *Contributions to Mineralogy and Petrology* **120**, 270–291.

Cocherie, A., Legendre, O., Peucat, J. J. & Kouamelan, A. N. (1998). Geochronology of polygenetic monazites constrained by *in situ* electron microprobe Th–U-total lead determination: implications for lead behaviour in monazite. *Geochimica et Cosmochimica Acta* **62**, 2475–2497.

Condie, K. C. (2000). Episodic continental growth models: afterthoughts and extensions. *Tectonophysics* **322**, 153–162.

Crowley, J. L. & Ghent, E. D. (1999). An electron microprobe study of the U–Th–Pb systematics of metamorphosed monazite: the role of Ph diffusion versus overgrowth and recrystallization. *Chemical Geology* **157**, 285–302.

Currie, K. L. & Gittins, J. (1988). Contrasting sapphirine parageneses from Wilson Lake, Labrador and their tectonic implications. *Journal of Metamorphic Geology* **6**, 603–622.

Dasgupta, S., Ehl, J., Raith, M. M., Sengupta, P. & Sengupta, P. (1997). Deep crustal contact metamorphism around the Chimakurthy mafic–ultramafic Complex, Eastern Ghats Belt, India. *Contributions to Mineralogy and Petrology* **129**, 182–197.

Dobmeier, C. & Raith, M. M. (2003). Crustal architecture and evolution of the Eastern Ghat Belt and adjacent regions of India. In: Yoshida, M., Windley, B. W. & Dasgupta, S. (eds) *Proterozoic East Gondwana: Supercontinent Assembly and Breakup. Geological Society, London, Special Publications* **206**, 145–168.

Dobmeier, C. & Simmat, R. (2002). Post-Grenvillian transpression in the Chilka Lake area, Eastern Ghats Belt: implications for the geological evolution of peninsular India. *Precambrian Research* **113**, 243–268.

Eriksson, P. G., Mazumder, R., Sarkar, S., Bose, P. K., Altermann, W. & van der Merwe, R. (1999). The 2·7–2·0 Ga volcano-sedimentary record of Africa, India and Australia: evidence for global and local changes in sea level and continental freeboard. *Precambrian Research* **97**, 269–302.

Fitzsimons, I. C. W. (1996). Metapelitic migmatites from Brattstrand Bluffs, East Antarctica: metamorphism, melting and exhumation of the mid crust. *Journal of Petrology* **37**, 395–414.

Fitzsimons I. C. W. & Harley, S. L. (1994). The influence of retrograde cation exchange, *P–T* estimates and a convergence technique for the recovery of peak metamorphic conditions. *Journal of Petrology* **35**, 543–576.

Fuhrman, M. L. & Lindsley, D. H. (1988). Ternary-feldspar modeling and thermometry. *American Mineralogist* **73**, 201–215.

Ganguly, J., Chakraborty, S., Sharp, T. & Rumble, D., III (1996). Constraint on the time scale of biotite grade metamorphism during Acadian orogeny from a natural garnet–garnet diffusion couple. *American Mineralogist* **81**, 1208–1216.

Goscombe, B. (1992). High-grade reworking of central Australian granulites: metamorphic evolution of the Arunta complex. *Journal of Petrology* **33**, 917–962.

Goscombe, B., Armstrong, R. & Barton, J. M. (1998). Tectonometamorphic evolution of the Chewore inliers: partial re-equilibration of high-grade basement during the pan-African orogeny. *Journal of Petrology* **39**, 1347–1384.

Harley, S. L. (1989). The origin of granulites: a metamorphic perspective. *Geological Magazine* **126**, 215–247.

Harley, S. L. (1998). On the occurrence and characterization of ultrahigh-temperature crustal metamorphism. In: Treloar, P. J. & O'brien, P. J. (eds) *What Drives Metamorphism and Metamorphic Reactions? Geological Society, London, Special Publications* **138**, 81–107.

Hensen, B. J. (1987). *P–T* grids for silica-undersaturated granulites in the systems MAS (n + 4) and FMAS (n + 3): tools for the derivation of *P–T* paths of metamorphism. *Journal of Metamorphic Geology* **5**, 255–271.

Hensen, B. J. & Harley, S. L. (1990). Graphical analyses of *P–T–X* relations in granulite facies metapelites. In: Ashworth J. R. & Brown, M. (eds) *High Temperature Metamorphism and Crustal Anatexis*. London: Unwin Hyman, pp. 19–56.

Holland, T. J. B. & Powell, R. (1998). An internally consistent thermodynamic dataset for phases of petrological interest. *Journal of Metamorphic Geology* **16**, 309–343.

Jain, S. C., Yedekar, D. B. & Nair, K. K. K. (1991). Central Indian shear zone: a major Pre-cambrian crustal boundary. *Journal of Geological Society of India* **37**, 521–531.

Kelly, N. M., Clarke, G. L. & Fanning, C. M. (2002). A two-stage evolution of the Neoproterozoic Rayner Structural Episode: new U–Pb sensitive high resolution ion microprobe constraints from the Oygarden Group, Kemp Land, East Antarctica. *Precambrian Research* **116**, 307–330.

Kovach, V. P., Simmat, R., Rickers, K., Berezhnaya, N. G., Salnikova, E. B., Dobmeier, C., *et al.* (2001). The Western Chamockite Zone of the Eastern Ghats Belt, India—an independent crustal province of late Archaean (2·8 Ga) and Palaeoproterozoic (1·7–1·6 Ga) terrains. *International Symposium and Field Workshop on the Assembly and Breakup of Rodinia and Gondwana, Osaka, 26–30 October 2001. Gondwana Research* **4**, 666–667.

Kretz, R. (1983). Symbols for rock-forming minerals. *American Mineralogist* **68**, 277–279.

Lippolt, H. J. & Hautmann, S. (1994). $^{40}Ar/^{39}Ar$ ages of Precambrian manganese ore minerals from Sweden, India and Morocco. *Mineralium Deposita* **18**, 195–215.

McDade, P. & Harley, S. L. (2001). A petrogenetic grid for aluminous granulite facies metapelites in the KFMASH system. *Journal of Metamorphic Geology* **19**, 45–59.

Mezger, K. & Cosca, M. A. (1999). The thermal history of the Eastern Ghats Belt (India), as revealed by U–Pb and $^{40}Ar–^{39}Ar$ dating of metamorphic and magmatic minerals: implications for the SWEAT correlation. *Precambrian Research* **94**, 251–271.

Mishra, D. C., Singh, B., Tiwari, V. M., Gupta, S. B. & Rao, M. B. S. V. (2000). Two cases of continental collisions and related tectonics during the Proterozoic period in India: insights from gravity modelling constrained by seismic and magnetotelluric studies. *Precambrian Research* **99**, 149–169.

Montel, J.-M., Fcret, S., Veschambre, M., Nicollet, C. & Provost, A. (1996). Electron microprobe dating of monazite. *Chemical Geology* **131**, 37–53.

Moraes, R., Brown, M., Fuck, R. A., Camargo, M. A. & Lima, T. M. (2002). Characterization and *P–T* evolution of melt-bearing ultrahigh-temperature granulites: an example from the Anápolis–Itauçu Complex of the Brasília Fold Belt, Brazil. *Journal of Petrology* **43**, 1673–1705.

Mouri, H., Guiraud, M. & Hensen, B. J. (1996). Petrology of phlogopite–sapphirine-bearing Al–Mg granulites from Ihouhaouene in Ouzzal, Hoggar, Algeria: an example of phlogopite stability at high temperature. *Journal of Metamorphic Geology* **14**, 725–738.

Nair, R. & Chacko, T. (2002). Fluid-absent melting of high-grade semipelites: *P–T* constraints on orthopyroxene formation and implications for granulite gneiss. *Journal of Petrology* **43**, 2121–2141.

Pandey, B. K., Krishna, V. & Chabria, T. (1998). An overview of Chotanagpur gneiss–granulite complex and adjoining sedimentary sequences, Eastern and Central India. In: *International Seminar on Precambrian Crust in Eastern and Central India*. UNESCO–IUGS–IGCP-368, pp. 131–135.

Patiño-Douce, A. E. & Beard, J. S. (1995). Dehydration melting of biotite gneiss and quartz amphibolite from 3 to 15 kbar. *Journal of Petrology* **36**, 707–738.

Pattison, D. R. M., Chacko, T., Farquhar, J. & McFarlane, C. R. M. (2003). Temperatures of granulite facies metamorphism: constraints from experimental phase equilibria and thermobarometry corrected for retrograde exchange. *Journal of Petrology* **44**, 867–900.

Rivers, T., Martignole, J., Gower, C. F. & Davidson, A. (1989). New tectonic divisions of the Grenville Province. southeast Canadian sheild. *Tectonics* **8**, 63–84.

Sengupta, P., Sen, J., Dasgupta, S., Raith, M., Bhui, U. K. & Ehl, J. (1999). Ultra-high temperature metamorphism of metapelitic granulites from Kondapalle, Eastern Ghats Belt: implications for the Indo-Antarctic correlation. *Journal of Petrology* **40**, 1065–1087.

Shulters, J. C. & Bohlen, S. R. (1989). The stability of hercynite and hercynite–gahnite spinels in corundum or quartz-bearing assemblages. *Journal of Petrology* **30**, 1017–1031.

Simmat, R. (2003). Identifizierung hochgradig metamorpher Provinzen des Eastern Ghats Belt in Indien anhand einer EMS-Studie von Monazit-Altersmustern. Ph.D. thesis, Universität Bonn.

St-Onge, M. R. & Ijewliw, O. J. (1996). Mineral corona formation during high-*P* retrogression of granulitic rocks, Ungava orogen, Canada. *Journal of Petrology* **37**, 553–582.

Stevens, G., Clemens, J. D. & Droop, G. T. R. (1997). Melt production during granulite-facies anatexis: experimental data from 'primitive' metasedimentary protoliths. *Contributions to Mineralogy and Petrology* **128**, 352–370.

Suzuki, K. & Adachi, M. (1991). Precambrian provenance and Silurian metamorphism of the Tsubonosawa paragneiss in the South Kitakami terrane, Northeast Japan, revealed by the chemical

Th–U-total Pb isochron ages of monazite, zircon and xenotime. *Geochemical Journal* **25**, 357–376.

Suzuki, K., Adachi, M. & Kajizuka, I. (1994). Electron microprobe observations of Pb diffusion in metamorphosed detrital monazites. *Earth and Planetary Science Letters* **128**, 391–405.

Vielzeuf, D. & Montel, J. M. (1994). Partial melting of metagreywackes. Part I: fluid-absent experiments and phase relationships. *Contributions to Mineralogy and Petrology* **117**, 375–393.

Vielzeuf, D. & Schmidt, M. W. (2001). Melting relations in hydrous systems revisited: application to metapelites, metagreywackes and metabasalts. *Contributions to Mineralogy and Petrology* **141**, 251–267.

Waters, D. J. (1989). Metamorphic evidence for the heating and cooling path of Namaqualand granulites. In: Daly, J. S., Cliff, R. A. & Yardley, B. W. D. (eds) *Evolution of Metamorphic Belts. Geological Society, London, Special Publications* **43**, 357–363.

Windley, B. F. (2003). Continental growth in the Proterozoic: a global perspective. In: Yoshida, M., Windley, B. F. & Dasgupta, S. (eds) *Proterozoic East Gondwana: Supercontinent Assembly and Breakup. Geological Society, London, Special Publications* **206**, 23–33.

Yedekar, D. B., Jain, S. C., Nair, K. K. K. & Dutta, K. K. (1990). The Central Indian Collision Suture. In: *Precambrian of Central India. Geological Survey of India, Special Publications* **28**, 1–37.